



**Stockholm  
University**

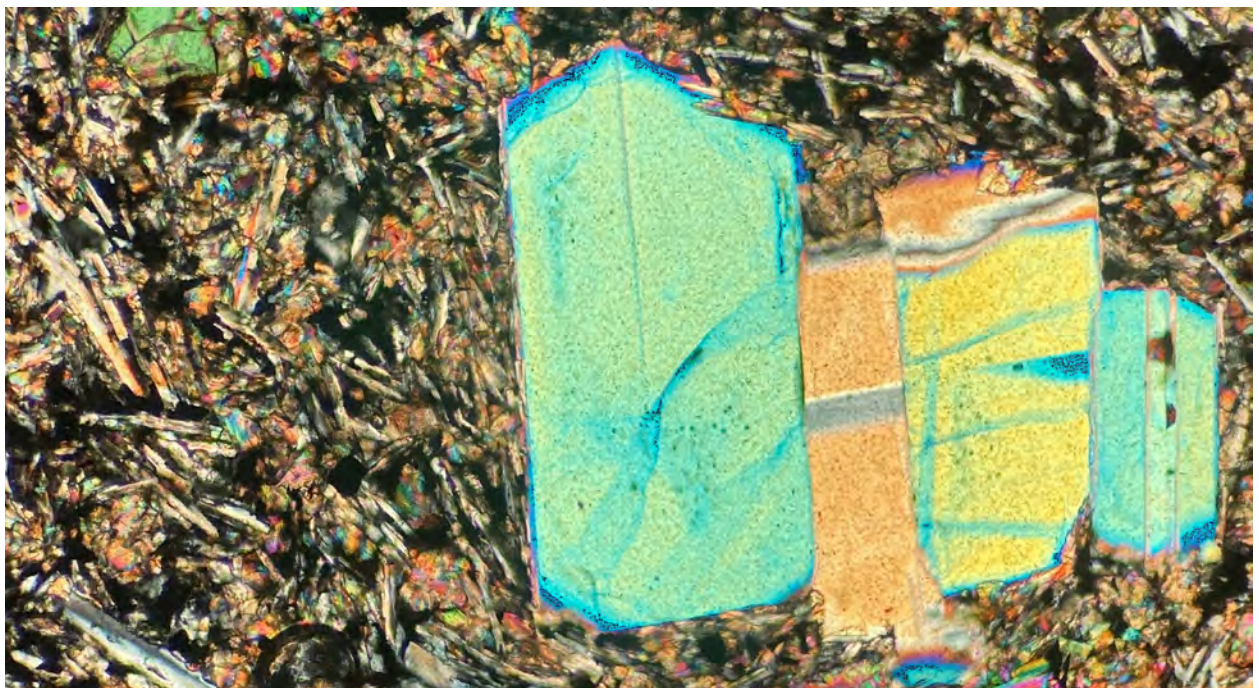
# Master Thesis

Degree Project in  
Geology 60 hp

## **A Feasibility Study of Carbon Sequestration in Basaltic Rock in Straumsvík, Iceland**

**A Petrological Characterisation of Basaltic Formations in the  
Stratigraphy of Monitoring Well CSM-01**

Daníel Pétursson



Stockholm 2025

Department of Geological Sciences  
Stockholm University  
SE-106 91 Stockholm

## Abstract

CO<sub>2</sub> injection into basaltic rocks is a promising method for permanent geological carbon storage. The Coda terminal project in Straumsvík, Iceland, explored this potential, but its success centres on a detailed understanding of the rock's petrological characteristics; however, limited research has been conducted previously specifically on the rock in the area. This study addresses that gap by carrying out a petrological characterisation of the basaltic stratigraphy from monitoring well CSM-01 and assesses its suitability for CO<sub>2</sub> sequestration. Well cutting samples and comparative fresh field samples were analysed using petrographic microscopy, whole-rock X-ray fluorescence (XRF) for major element geochemistry, normative mineral calculations, and modal point counting to quantify mineral phases. Results show that the stratigraphy is primarily composed of fine- to medium-grained tholeiitic basalt, characterised by low initial alteration and the presence of olivine phenocrysts, with lava flows that are interbedded with sedimentary horizons. Based on grain size and texture, the basalts were classified into three suites: a porphyritic glassy basalt, a porphyritic intergranular basalt, and a medium- to coarse-grained seriated basalt. Petrographic observations, point-counting data, and Loss on Ignition (LOI) values reveal a trend of increasing alteration with depth. This study concludes that the interval between 318 and 372 m depth in well CSM-01 is the most promising target for CO<sub>2</sub>-enriched fluid injection, offering the optimal combination of reactive phases (e.g., olivine, pyroxene, and fine-grained to glassy groundmass) and sufficient porosity for a successful carbon sequestration.

## Acknowledgements

I would like to thank the people and institutions who have helped me throughout this project. This master's thesis was made possible through the support from the Vísindag frumkvöðlasjóður Orkuveitunnar (VOR) grant and funded by Stockholm University. I was so fortunate to be awarded this grant, enabling me in my research, and I want to thank them for their investment in this research. I want to thank Carbfix for their collaboration on this project and giving me access to their samples to examine. I owe a special debt of gratitude to my supervisors. My main supervisor, Alasdair Skelton, provided me guidance in need, and I am grateful for his support throughout the project. My co-supervisor, Victoria Pease, who helped and taught me the practical matters of sample preparation and offered insightful perspectives that greatly improved the quality of this work. For their technical expertise, I thank Vancouver Petrographics for the preparation of the thin sections, and I want to thank Krister for her help in the making of the epoxy moulds for thin-sections. Again, I would like to thank the collaboration with Carbfix, and in particular, I thank Iwona Galeczka for her essential role in our partnership. I am grateful to my writing group—Flo, Moritz, and Truly—for their constructive feedback and motivation to see this project through. Heartfelt thanks also to my friends and colleagues at Stockholm University. I also want to thank Gísli Héðinsson for his sledgehammer. I want to thank my mom and dad for their support in my field sampling and in allowing me to use their car. I would also like to acknowledge the use of generative AI tools (such as Google's Gemini and OpenAI's ChatGPT) as a writing assistant. These tools were used exclusively for the purposes of improving grammar, writing code for figures, refining prose, and ensuring clarity in my writing. All substantive ideas, research, analysis, and conclusions presented in this thesis are entirely my own. This work would not have been possible without the contributions of many, but any errors that remain are my own.

## Contents

<b>1</b>	<b>Introduction</b>	<b>1</b>
1.1	Climate Change . . . . .	1
1.2	Carbon Capture and Storage (CCS) . . . . .	1
1.3	Optimising Carbon Storage . . . . .	3
1.4	The Sequestration Project and this Study . . . . .	4
<b>2</b>	<b>Geological Background</b>	<b>6</b>
2.1	Geology of Iceland . . . . .	6
2.1.1	Rift Plate Boundary . . . . .	6
2.1.2	The Volcanic Zones and Volcanic Systems . . . . .	6
2.1.3	Volcanism During Glacial and Interstadial Periods . . . . .	7
2.1.4	Composition of Eruptive Material . . . . .	8
2.2	Reykjanes Peninsula . . . . .	8
2.2.1	Volcanic Composition . . . . .	9
2.3	The Study Area . . . . .	10
<b>3</b>	<b>Methods</b>	<b>11</b>
3.1	Sample Collection . . . . .	11
3.1.1	Fieldwork . . . . .	11
3.1.2	Monitoring well Cuttings Collection and Logging . . . . .	11
3.2	Sample Preparation . . . . .	11
3.2.1	Thin-Section Preparation . . . . .	12
3.2.2	Loss on ignition (LOI) and X-Ray fluorescence (XRF) Preparation . . . . .	12
3.3	Analytical Techniques . . . . .	12
3.3.1	Loss on Ignition (LOI) . . . . .	12
3.3.2	X-Ray Fluorescence Spectrometer (XRF) . . . . .	13
3.3.3	Cross, Iddings, Pirsson, Washington (CIPW) Norm Calculations . . . . .	13
3.3.4	Point Counting . . . . .	13
3.3.5	Availability of Supplementary Data . . . . .	14
<b>4</b>	<b>Results</b>	<b>15</b>
4.1	Lithology . . . . .	15
4.1.1	Lithology of Field Samples . . . . .	15
4.1.2	Lithology of Monitoring Well CSM-01 . . . . .	16
4.2	Petrography . . . . .	19
4.2.1	Porphyritic Glassy Basalt . . . . .	20
4.2.2	Porphyritic Intergranular Basalt . . . . .	22
4.2.3	Medium- to Coarse-grained Basalt . . . . .	22
4.3	Geochemistry . . . . .	24
4.3.1	Total Alkali Silica (TAS) Classification . . . . .	26
4.3.2	Alkali Iron Magnesium Diagram (AFM) . . . . .	27
4.3.3	MgO against Oxides . . . . .	27

---

4.3.4	LOI . . . . .	31
4.4	Normative Calculations and Point Counting . . . . .	31
4.4.1	CIPW normative calculations . . . . .	31
4.4.2	Point Counting . . . . .	33
<b>5</b>	<b>Discussion</b>	<b>35</b>
5.1	Lithological Characterisation and Implications for Fluid Flow . . . . .	35
5.2	Mineralogy and its Suitability for Carbon Sequestration . . . . .	36
5.3	Grain Size and Textural Influences on Reactivity . . . . .	37
5.4	Alteration: Extent and Impact on Sequestration Potential . . . . .	38
5.5	Synthesis: Optimal Depths and Formations for Carbon Sequestration in Straumsvík . . . . .	39
5.6	Limitations of the Study . . . . .	40
<b>6</b>	<b>Conclusions and Recommendations</b>	<b>42</b>
6.1	Conclusions . . . . .	42
6.2	Recommendations for Future Work . . . . .	42

## List of Tables

1	CIPW normative calculation results of samples (vol.%). Abbreviations: plag: plagioclase, or: orthoclase, di: diopside, hy: hypersthene, ol: olivine, ilm: ilmenite, mag: magnetite, ap: apatite, adding up to 100% volume. . . . .	32
2	Modal mineral compositions (area%) from point counting. Abbreviations: plag: plagioclase, px: pyroxene, ol: olivine, gm: groundmass, ox: opaque oxides, alt: other alteration products. . . . .	34
3	Qualitative ranking of basalt units in CSM-01 and field samples for carbon sequestration potential. Where reactive mineralogy, grain size/texture, alteration state, and overall suitability are described in terms of suitability, VH: very high suitability H: high suitability, M: moderate suitability, L: low suitability, and V: variable (Based on data in Results). The colours correspond to the ranking: bright green is high suitability, olive green is moderate to good suitability, orange is moderate suitability and grey is variable and less suitable. . . . .	40

## List of Figures

- 1 Northern Reykjanes Ridge: NRR, Western Rift Zone (WRZ), Northern Rift Zone (NRZ), Snæfellsnes Volcanic Zone (SVZ), Eastern Rift Zone (ERZ), Mid-Iceland Belt (MIB), and Öräfajökull Belt (ÖB). The Reykjanes Peninsula is outlined with a black rectangle. This map is edited from Denk et al.'s (2011) map. . . . . 7
- 2 Study area (blue star), NRR and its six volcanic systems (orange), geothermal areas (yellow) and seismic belts (red). The map is based on Ísor's geological map (Sæmundsson et al., 2010). . . . . 9
- 3 A map of the lavas in study area of the Straumsvík region ordered in chronological age from the top of the legend. The red triangle is the drill hole, the red diamonds are analysed sample sites, and black points are not analysed sample sites. The map is based on ÍSOR's geological map (Sæmundsson et al., 2010) . . . . . 10
- 4 Fresh surface of rock sample PD-STV-24-01, the sample shows high vesicularity and a few plagioclase phenocrysts (white specs within the grey mass). The hammerhead's length is 15 cm. . . . . 15
- 5 Log of monitoring well CSM-01, represented in three columns: topmost 200 m on the left, 200-400 m in the middle, and on the right 400-600 m. Every cell represents 3 m of depth. Orange stars represent where samples were analysed. Oxidation levels are represented by colours: level 0 as white (none), level 1 as light red (mild), level 2 as red (moderate), and level 3 as dark red (considerable). . . . . 19
- 6 A, B, and C are PP, and D, E, and F are XP. Micrographs A and D show sample PD-STV-24-11. Micrographs B and E show sample CSM-01-372m. Micrographs C and F show sample CSM-01-600m. Abbreviations: Plag: plagioclase, Ol: olivine, Cpx: clinopyroxene, Ox: opaque oxides, Gm: groundmass, Ves: vesicle, Alt: alteration. The scale line (200  $\mu\text{m}$ ) applies to all micrographs. . . . . 21
- 7 A, B, and C are PP, and D, E, and F are XP. Micrographs A and D show sample PD-STV-24-03. Micrographs B and E show sample CSM-01-51m. Micrographs C and F show sample CSM-01-348m. Abbreviations: Plag: plagioclase, Ol: olivine, Cpx: clinopyroxene, Ox: opaque oxides, Alt: alteration. The scale line (200  $\mu\text{m}$ ) applies to all micrographs. . . . . 23
- 8 A, B, and C are PP, and D, E, and F are XP. Micrographs A and D show sample PD-STV-24-14. Micrographs B and E show sample CSM-01-258m. Micrographs C and F show sample CSM-01-294m. Abbreviations: Plag: plagioclase, Ol: olivine, Cpx: clinopyroxene, Ox: opaque oxides, Vs: vesicle, Alt: alteration. The scale line (200  $\mu\text{m}$ ) applies to all micrographs. 25

9	TAS (wt. %) diagram of the field samples in light green circles, and the samples from monitoring well CSM-01, with shallow (18-306 m) samples as light blue squares, intermediate depth samples (318-405 m) as blue diamonds, and deep-well samples (546-600 m) as purple triangles (Le Bas et al., 1986). . . . .	26
10	AFM ( $\text{Na}_2\text{O} + \text{K}_2\text{O}$ , $\text{FeO}_{\text{total}}$ , and $\text{MgO}$ , all in wt.%) diagram illustrating the tholeiitic affinity of the analysed samples. The dividing line between tholeiitic and calc-alkaline fields is after Vermeesch and Pease (2021). Symbols represent field samples (light green circles), shallow well cuttings (18-306 m; light blue squares), intermediate well cuttings (318-405 m; Blue diamonds), and deep-well cuttings (546-600 m; purple triangles). . . . .	27
11	Harker diagrams with $\text{MgO}$ (wt.%) on x-axis and in the left column of $\text{SiO}_2$ , $\text{Na}_2\text{O}$ , $\text{CaO}$ , and $\text{TiO}_2$ (all in wt.%) in y-axis. In the right column, $\text{P}_2\text{O}_5$ , $\text{K}_2\text{O}$ , $\text{Al}_2\text{O}_3$ , and total Fe (sum of $\text{FeO}$ and $\text{Fe}_2\text{O}_3$ , wt.%). Samples are differentiated by depth and correspond to field samples (light green circles), shallow well samples (18-306 m; light blue squares), intermediate well samples (318-405 m; blue diamonds), and deep well samples (546-600 m; purple triangles). . . . .	28
12	LOI (wt.%) plotted against depth with lithological log, shallow well samples (18-306 m) are light blue squares, intermediate well samples (318-405 m) are blue diamonds, and deep well samples (546-600 m) are purple triangles. the average of LOI values in field samples (excluding PD-STV-24-14) are shown in bright green vertical line, while the value of PD-STV-24-14 is shown in faint green vertical line; the dashed vertical line is 0 wt.% . . . . .	30

# 1 Introduction

## 1.1 Climate Change

Anthropogenic greenhouse gas emissions of CO<sub>2</sub> in particular have been strongly linked with the increase in global average temperatures since the 20th century, and climate models highlight the urgency to reduce further warming (Calvin et al., 2023). Despite international commitments under the Paris Agreement, emission reductions alone are insufficient to stay on the target to keep the “increase in the global average temperature well below 2 °C above pre-industrial levels” (United Nations, 2015). The global temperature had already risen 1.1 °C between 2011 and 2020, according to the Intergovernmental Panel on Climate Change (IPCC) (Calvin et al., 2023). To meet the climate targets, technologies for carbon capture and storage (CCS) are recognised as an essential cog in the emission reductions.

## 1.2 Carbon Capture and Storage (CCS)

Carbon capture and storage, or CCS for short, refers to technologies for the removal of CO<sub>2</sub> from ambient air or point sources of CO<sub>2</sub> emissions, transportation, and storage with the goals of preventing or reversing CO<sub>2</sub> releases into the atmosphere (*Global Status of CCS Report*, 2018). While numerous CCS strategies have been explored, scaling remains the critical challenge. CCS methods are strongly driven by the economic benefits of their use. The dominance of oil and gas in major CCS projects highlights this driver. For wider adoption of CCS, efforts backed by governments—through subsidies, regulations, and legislation—need to be implemented (The International Energy Agency, 2020).

There are two approaches for capturing CO<sub>2</sub>: either at the source of large industrial sources of emission, called point source capture, or directly from ambient air, otherwise known as direct air capture (DAC). After capture, about 90% of the CO<sub>2</sub> is transported and utilised in the oil and gas industry, the food and beverage industry, or for chemical production (The International Energy Agency, 2019).

For a successful approach to storage of CO<sub>2</sub>, it is essential to understand the carbon cycle and its reservoirs. The Earth systems (atmo-, bio-, hydro-, cryo-, and lithosphere) provide different reservoirs. The lithosphere is by far the largest reservoir for long-term storage of carbon. That’s why CCS projects that utilise geological environments and processes of the lithosphere are essential for a sustainable future (Golubić et al., 1979). Today there are two main methods of storing CO<sub>2</sub> long-term. Firstly, by storing structurally beneath cap rock and secondly, by mineral sequestration as solid carbonates. Both utilise the lithosphere for storage, and with time the storing systems become more secure, and the carbon is incorporated into the rock (Solomon, 2007; Deng et al., 2017; Alcalde et al., 2018; Snæbjörnsdóttir et al., 2020).

The more conventional method of carbon storage is by injecting supercritical CO<sub>2</sub> (scCO<sub>2</sub>) beneath caprock, where the trapping of the CO<sub>2</sub> is mainly structural, for example, in Equinor’s project Sleipnir in Norway (*Global Status of CCS Report*, 2018). These

environments are oil reservoirs, deep saline basins, and organic-rich shale basins (Bodnar et al., 2013). Theoretically, with time the  $\text{CO}_2$  dissolves into brines, which happens on timescales of tens to hundreds of years. And after hundreds to tens of thousands of years, 20% of injected  $\text{CO}_2$  may be mineralised (Bodnar et al., 2013). The oil and gas industry uses  $\text{CO}_2$  for enhanced oil recovery (EOR). The EOR utilisation leads to storage of the  $\text{CO}_2$  under caprocks in porous rocks that previously hosted by oil and gas in pores. Security against leakage is debated due to the mechanisms by which the  $\text{CO}_2$  is trapped (i.e., as a supercritical fluid ( $\text{scCO}_2$ ) under sedimentary caprock, with limited dissolution in brine) and the financial drivers for the industry to claim the method as a secure long-term storage of  $\text{CO}_2$ . Other, more secure methods of carbon storage must be established. All major CCS operations (in Mtonnes/year) are carried out by the oil and gas industry, which initially adopted the method for enhanced oil recovery (EOR). The  $\text{scCO}_2$  replaces the wanted resources in pores for increased pressure in the reservoir, making it easier to extract. Norway has dedicated geological storages at sea, where  $\text{scCO}_2$  is injected into sandstone at depth under sedimentary caprocks. There are variations in the methods depending on the geological environments; for example, in some projects,  $\text{scCO}_2$  is injected into brine-rich reservoirs, leading to the dissolution of the fluid. There are claims that over time this method of trapping  $\text{scCO}_2$  under caprock becomes more secure as  $\text{scCO}_2$  dissolves into brines over hundreds to thousands of years and later mineralises into carbonates over thousands to millions of years, but this remains to be proven. Major concerns are leakage and movement of the  $\text{scCO}_2$  with this method. Whether this withstands scrutiny only becomes evident over time (Bodnar et al., 2013).

While structural storage offers a promising initial solution, the potential for leakage and movement necessitates the exploration of more permanent solutions. Recent advances in mineral sequestration, particularly in reactive mafic rock systems, offer a pathway to permanent  $\text{CO}_2$  storage without requiring structural trapping. The main difference between the two methods is that dissolved  $\text{CO}_2$  and fluid-rock interaction at depth are exploited to form carbonate minerals. Consequently, the storage method is faster than the traditional cap rock method, within ten years, and studies report a significant sequestration within 2 years (Matter et al., 2016; Snæbjörnsdóttir et al., 2020). The apparent risk of leakage remains minimal, but with the timescale of mineralisation, it varies depending on methods of injection of the fluid and properties of the rock.

A good example of the mineral sequestration method used in the field (by Carbfix) is  $\text{CO}_2$  injections with water, where the gas dissolves into the fluid on the way down through boreholes into a few hundred metres deep basalt formations, where fluid-rock interactions mineralise  $\text{CO}_2$ . The low-pH carbonated water flows into the rock's pores and along permeable pathways. Close to the injection zone, conditions are more acidic, and the rock tends to dissolve, introducing divalent cations, e.g.,  $\text{Ca}^{2+}$ ,  $\text{Mg}^{2+}$ , and  $\text{Fe}^{2+}$  to the injected fluid. Further from the injection zone, the cations bond to the carbonate species, forming carbonate minerals, calcite being the most abundant mineral formed in Icelandic basalt conditions. Furthermore, if it is not mineralised, the carbonate species

will stay dissolved at depth because of pressure dissolution and because the CO<sub>2</sub>-enriched fluid is less buoyant than natural groundwater (Marini, 2006; Matter et al., 2016; Clark et al., 2020; Galeczka et al., 2022).

### 1.3 Optimising Carbon Storage

Fluid-rock interaction is paramount for optimisation of carbon storage. To maximise this, research suggests that rocks need to have reactive minerals with available divalent cations, fine-grained textures to efficiently trap CO<sub>2</sub> as stable carbonates, and high porosity and permeability for a high rock-to-water ratio and efficient flow of the fluid through the rock (Israeli and Emmanuel, 2018).

The composition of the fluid is the most controllable factor, but when injected at depth, it mixes with groundwater, which makes the fluid's behaviour less predictable. Given that the fluid's composition is controllable, it is enriched in CO<sub>2</sub>, forming carbonic acid and lowering the pH. The increased acidity makes the surrounding rock more susceptible to dissolution, facilitating the release of divalent cations from minerals.

The chemical composition of the rock is important as a source of the divalent cations (Ca<sup>2+</sup>, Mg<sup>2+</sup>, Fe<sup>2+</sup>) needed to form the carbonate minerals. Basalt is rich in these reactive minerals, with its basic composition of major minerals being plagioclase, pyroxene, and olivine. Basaltic glass, an amorphous phase of the rock, further enhances the reactivity as it lacks crystalline structure (Oelkers and Gislason, 2001; Gislason and Oelkers, 2003).

The texture of the rock contributes to its reactivity. Finer-grained minerals provide a greater surface area for reactions, thereby enhancing reactivity. Such rocks also tend to contain higher proportions of volcanic glass. Additionally, the degree of alteration influences the reactive potential of the rock. Unaltered rocks have significantly higher leaching rates than altered ones (Gislason & Oelkers, 2003). Icelandic basalts are fine-grained in most cases and are often unaltered or only altered to a limited degree.

Permeability and porosity of a rock are essential for efficient fluid-rock interaction. High permeability between rock layers and vesicularity and porosity of the rock allow for greater contact area between the rock and fluid. The greatest permeability in basalt flows occurs between flows where scoraceous and rubbly material make the formation porous. Moreover, most basalt is vesicular and therefore has high porosity. This allows large areas of the rock to be in contact with the fluid (Luhmann et al., 2017). Furthermore, vesicularity can serve as an analogue for porosity in Icelandic basaltic rocks, as Sigurdsson and Stefansson (2002) showed that vesicularity between 0–50% typically aligns within  $\pm 2\%$  of effective porosity measurements. This correlation holds when vesicles dominate the pore space and secondary porosity (e.g., fractures, microcracks) is negligible (O. Sigurdsson & Stefansson, 2002). As acidic fluid permeates the formation, it accesses a large volume of rock and increases the contact area for reactions to occur.

Basalt, an extrusive volcanic rock, exhibits each of these beneficial properties. It is typically fine-grained, its composition including the minerals pyroxene and olivine and often glass, and has high permeability and vesicularity, which enhances fluid-rock

interactions. This rock is therefore particularly suitable for carbon sequestration by mineralisation. Carbfix's studies indicate that 95% of CO<sub>2</sub> injected is mineralised within two years. The effectiveness of the Carbfix method was validated through the use of reactive and non-reactive tracers, along with ratios of isotope signatures of carbon (C<sup>12</sup> and C<sup>14</sup>) and calcium (Ca<sup>40</sup> and Ca<sup>44</sup>) (Matter et al., 2016; Pogge von Strandmann et al., 2019). Furthermore, a pilot project in Wallula, USA, successfully injected 1000 tonnes of scCO<sub>2</sub>. Monitoring of groundwater and soil gas, complemented with ground deformation imaging, showed no leakage of the CO<sub>2</sub> (McGrail et al., 2011).

#### 1.4 The Sequestration Project and this Study

Through the years, Carbfix has worked on a carbon sequestration method through research projects and now has a method ready to upgrade to the Megatonne scale. The CODA Terminal in Straumsvík, Iceland, is a collaboration project between Carbfix and Dan-Unity CO<sub>2</sub> to scale injection of CO<sub>2</sub> to the Megatonne scale (3 Mtonne) by importing CO<sub>2</sub> by sea from Europe to the injection site in Straumsvík, Iceland.

Carbfix's Coda terminal project in Straumsvík faced public opposition and a decision was made to withdraw from the project in that area to maintain a positive public image for environmental projects. Although the project's progression was paused, the drilling of monitoring well CSM-01 provides a critical opportunity to assess the site's petrological suitability for future carbon storage initiatives. Carbfix still has the Straumsvík area in mind for future projects. The CODA terminal project could be an important contribution to CCS efforts. To meet the IPCC's projected requirement of sequestering up to 20 gigatonnes (Gt) of CO<sub>2</sub> annually by 2040, approximately 2,500 dedicated CCS projects will need to be operational. The scalability of these projects is paramount (*Global Status of CCS Report*, 2018). What Carbfix in Iceland offers is a vast amount of basalt ready to store CO<sub>2</sub> for the foreseeable future. The area of Iceland contains basalt formations capable of storing 2500 Gtonnes of CO<sub>2</sub>. Carbfix's Coda terminal project has the goal to sequester 3 Mt of CO<sub>2</sub> annually in its last phase, 2023 (Galeczka, 2023; Kristjánsdóttir et al., 2024; Myer et al., 2024). Even though Carbfix has done a lot of research on life cycle assessments, groundwater chemistry, seismicity, and geochemical modelling, the Carbfix Coda Terminal project has not done a thorough petrological analysis of the rock to be injected with CO<sub>2</sub>. Such a study is crucial for optimising injection strategies and understanding long-term CO<sub>2</sub> behaviour in the reservoir rock.

While reaction rates have been established for individual mineral phases, permeability and reaction path models have been made (Oelkers and Gislason, 2001; Gislason and Oelkers, 2003; Galeczka et al., 2022; Galeczka, 2023; Delerce et al., 2024; Wang et al., 2024), while the rock's texture, such as grain size and degree of alteration, significantly impacts overall reactivity. The aim of this study is to provide a comprehensive petrological, geochemical, mineralogical, and textural characterisation of the basaltic formations in the stratigraphy of the Straumsvík region with drill-hole cuttings from CSM-01 and corresponding field samples and to assess the carbon uptake quality of the rock, i.e., suitability for forming carbonate minerals. The study's second target is to determine

the depth at which it would be most applicable to inject the CO<sub>2</sub>-enriched fluid for the most effective carbon uptake in the Straumsvík area, based on these results. The overarching goal is making a baseline for future comparison with projects post-injection.

## 2 Geological Background

### 2.1 Geology of Iceland

Iceland is a 103000 km<sup>2</sup> volcanic island in the middle of the North Atlantic Ocean. The volcanic activity is due to the interplay of the mid-oceanic ridge and mantle upwelling. This upwelling, often called a mantle plume, feeds volcanic matter from beneath the Earth's crust to the surface, resulting in generally primitive volcanic material. On the Atlantic Mid-Oceanic Ridge, the American plate in the NW and the Eurasian plate in the SE meet (Schilling, 1973; Wolfe et al., 1997; Howell et al., 2014). As they separate at the plate boundary in Iceland, a series of seismic and volcanic rift zones form from the SW peninsula to the NE part of the island and extend far into the north and south of it (Sigmundsson et al., 2020).

#### 2.1.1 Rift Plate Boundary

The plates are gradually spreading apart; in Iceland this manifests itself in 18.2 mm/y spreading on average in the 105° NWW-SEE direction (P. Einarsson, 2008). Tectonic and some volcanic activities are then a consequence of the spreading. Iceland's tectonic activity can be categorised into four different zones: rift zones, of crustal spreading and volcanism producing the tholeiitic crust of Iceland; fracture zones, non-volcanic regions marked with strike-slip faulting joining the misaligned spreading zones; trans-tensional zones, with both strike-slip and normal fault movement and volcanism; and flank zones, systems outside the spreading zones overlaying the tholeiitic crust with transitional alkalic to alkalic rocks and associated with minor rifting (Sæmundsson et al., 2018). Due to the spreading, the oldest (14-16 Ma) on-land rocks are found in the Westfjords and Eastfjords (Hardarson et al., 2008).

#### 2.1.2 The Volcanic Zones and Volcanic Systems

The active rift zones are comprised of long fissure swarms that extend for tens of km. The volcanic zones, the active volcanic zones along the plate boundary, are divided into the Northern Reykjanes Ridge (NRR), Western, Eastern, and Northern Rift Zones (WRZ, ERZ, and NRZ), which join at the Mid-Iceland Belt (MIB) at the rift zones. The activity of the rift zones is accommodated along a segmented and curvilinear alignment. Specifically, the NRZ exhibits an N-S trend, transitioning to an SW-NE orientation in the central part and then to a W-E alignment on the Reykjanes Peninsula (on the northernmost part of NRR) (see in Figure 1). The Snæfellsnes Volcanic Zone (SVZ) and Öraefajökull belt (ÖB) are in the flank zones. Around 30 volcanic systems are associated with these zones, generally consisting of dike swarms and a central volcano. These central volcanoes can vary greatly, but most of them have in common an evolved eruptive material, a fissure swarm, and high-temperature geothermal systems (Sæmundsson, 1991; Thordarson and Larsen, 2007; P. Einarsson, 2008; Jakobsson et al., 2008; Denk et al., 2011; Sæmundsson et al., 2018). Within some central volcanoes, calderas have developed. (S. Einarsson et al., 1991; Thordarson and Larsen, 2007; Hjartardóttir et al.,

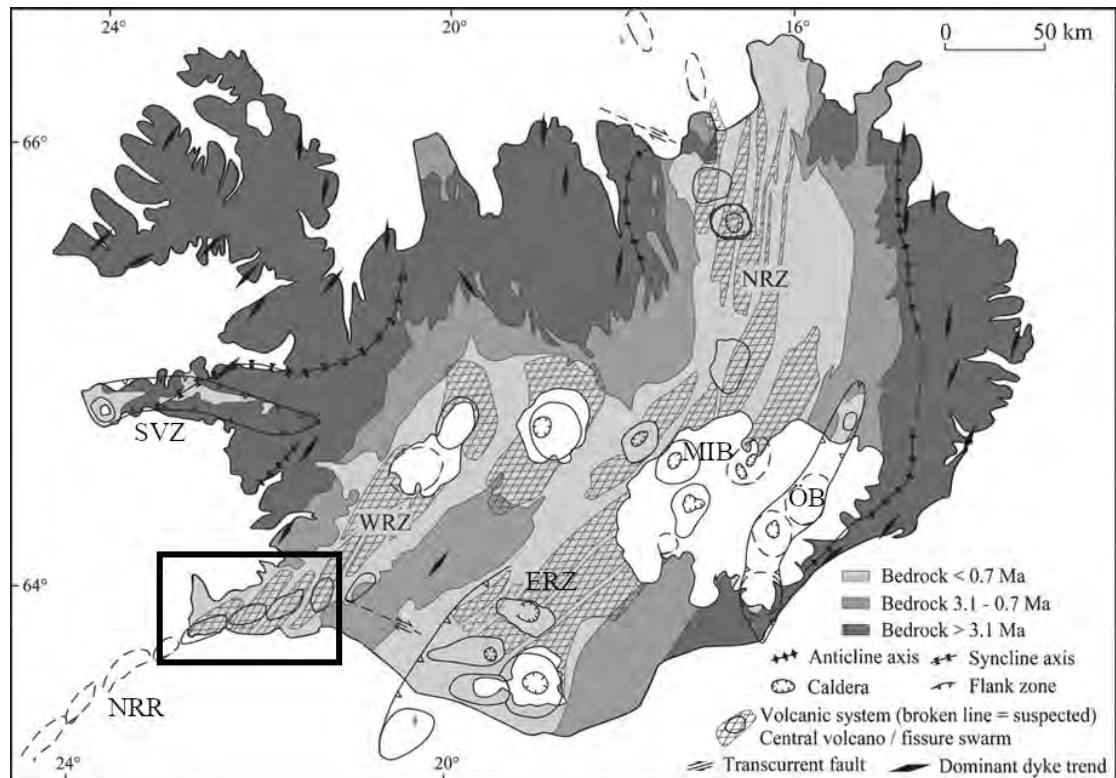


Figure 1: Northern Reykjanes Ridge: NRR, Western Rift Zone (WRZ), Northern Rift Zone (NRZ), Snæfellsnes Volcanic Zone (SVZ), Eastern Rift Zone (ERZ), Mid-Iceland Belt (MIB), and Öraefajökull Belt (ÖB). The Reykjanes Peninsula is outlined with a black rectangle. This map is edited from Denk et al.'s (2011) map.

2016). The NRR deviates from most of the volcanic zones as the volcanic systems do not produce highly evolved material and do not have a central volcano with a caldera (Sæmundsson et al., 2018).

### 2.1.3 Volcanism During Glacial and Interstadial Periods

Crystal size in volcanic rocks depends on the rate of cooling of the rock, and topography can have a big influence on the cooling rate depending on if the lavas flow into valleys or in a relatively flat area. During glacial periods the volcanic material produced on land is mostly hyaloclastite, consisting of fragmented pillow lavas erupted beneath the glaciers. The rocks contain glassy and fine-grained fragments, but the major elemental composition is essentially the same as during interstadial periods. During interstadial periods, volcanism increases due to depressurisation of the crust during its isostatic rebound (Gee et al., 1998; Slater et al., 1998; MacLennan et al., 2002). The flowing basaltic lava fills in the deep valleys left by the erosion of the glaciers, and the thick lavas cool more slowly, leading to more coarse-grained rocks. These rocks are often called "grágrýti" or "grey rocks" due to their grey appearance. The local deglaciation (14,500–12,500 yr BP) of the Reykjanes peninsula increased eruption rates by a factor of 100. The rocks decreased in light REEs content by 15 % during that period (Gee et al., 1998). Gee et al. (1998) argued that this change in trace elements was due to

shorter residence time of melt in the crust and indicated increased magma melting at greater depth.

#### 2.1.4 Composition of Eruptive Material

Volcanic rocks in Iceland range in composition from basaltic to rhyolitic. According to Jakobsson et al. (2008), the abundance of them is as follows: 75% basalts, 14% intermediate rocks, and 11% silicic rocks. The chemical composition of Icelandic eruptive material is categorised into three series: alkalic, transitional alkalic, and tholeiitic series. There can be overlap between the series because of natural variability and magma mixing (Le Maitre, 2002; Maclennan et al., 2002; Jakobsson et al., 2008). The majority of Icelandic basalts are tholeiitic. The rift zones NRR, WVZ, and NVZ are tholeiitic, while the flank zones EVZ, SVZ, and the Öraefajökull belt range from tholeiitic to alkalic (see Figure 1). The tholeiitic series are high in Fe and Ti content and low in Al content. They have higher contents of Ti compared to Mid-Ocean Ridge Basalts (MORBs) and always plot below the TAS Hawaiian division line (4-5 wt.% alkali content) (Jakobsson et al., 2008). The basaltic rocks of this series comprise picrite, olivine tholeiite, and tholeiite. The picrites are defined as containing 12-18 wt.% MgO, and the SiO<sub>2</sub> content is always >45 wt.% (Jakobsson et al., 2008). Olivine tholeiite has a greater abundance of olivine than tholeiite and therefore also has higher MgO content.

## 2.2 Reykjanes Peninsula

Reykjanes Peninsula is the only on-land example of a trans-tensional and rifting zone in Iceland, evident in the N-S trending right-lateral transform faults. The zone has a correspondent zone off the coast of north Iceland, the Tjörnes fracture zone (Sæmundsson et al., 2018). On the surface, the Reykjanes Peninsula exhibits fractures created after tectonic movements. They are not distributed evenly over the peninsula but rather appear in fracture zones, that is, elongated systems composed of offsets, fractures, faults, and other landforms associated with tectonic movements that are mostly parallel and align with the volcanic fissures (P. Einarsson & Imsland, 2013). These systems are connected to the volcanic belt but often extend several tens of kilometres out of it. The volcanic systems trend NE-SW and are manifested by geological features such as craters, crater rows, and fissures in the volcanic systems of the peninsula. There are six volcanic systems in the NRR, counted from the west: Reykjanes, Eldvörp-Svartsengi, Fagradalsfjall, Krýsuvík, Brennisteinsfjöll, and Hengill (see Figure 2). The characteristics of these deviate from the general volcanic systems of Iceland. Only the easternmost system, Hengill, has all the traditional features of a volcanic system. The other systems lack a central volcano with a developed caldera. Excluding the Hengill system, the systems strictly produce tholeiitic mafic material. Fagradalsfjall is the only system without fissure swarms and geothermal activity on the surface (Sæmundsson et al., 2018). This area is very interesting for studies on carbon sequestration, as the stratigraphy is predominantly made up of reactive basaltic rock.

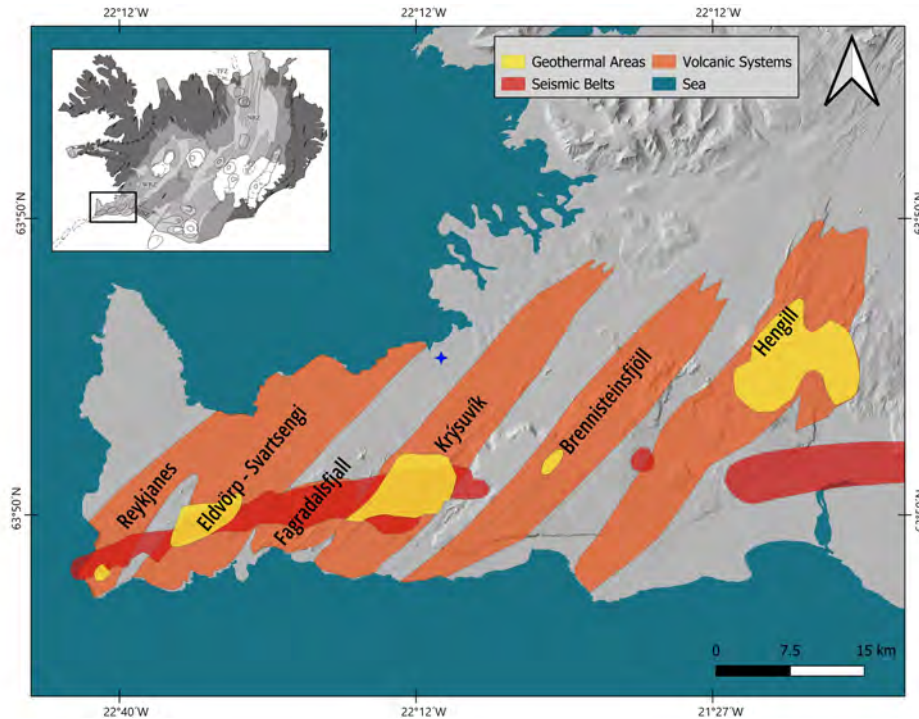


Figure 2: Study area (blue star), NRR and its six volcanic systems (orange), geothermal areas (yellow) and seismic belts (red). The map is based on Ísor's geological map (Sæmundsson et al., 2010).

### 2.2.1 Volcanic Composition

The most evolved volcanic material from the volcanic systems of the peninsula is evolved basalt, excluding the Hengill system. After the deglaciation of the peninsula (14 ka BP), the group divided into small picrite basalt lava shields, large olivine tholeiite lava shields, and tholeiite fissure lavas, which formed in that order (Jakobsson et al., 1978). They are characterised by a low content of alkalis and high CaO. There is a positive correlation between the volume of individual lavas and the content of incompatible elements of the lavas within each group. Likewise, there is an overall chemical trend through time demonstrated by a rise in  $K_2O$  from about 0.02% to 0.24% during the last approximately 12000 years (Jakobsson et al., 1978). The basaltic rocks consist mainly of plagioclase, olivine, and pyroxene (px). In the tholeiitic series, the orthopyroxene hypersthene has a normative (CIPW) value of 10 to 20%. Two clinopyroxenes, augite and pigeonite, are found in the ground mass of these rocks (Nicholson, 1991; Martin and Sigmarsson, 2007). Olivine phenocrysts are common in picrites and fairly common in olivine tholeiites and tholeiites. Oxides like ilmenite, magnetite, and chromite are common accessory minerals in the mafic rocks of the tholeiitic series (Gee et al., 1998; I. A. Sigurdsson et al., 2000). The abundance of plagioclase macrophenocrysts varies between the volcanic systems of the peninsula, and macrophenocrysts of augite are rare (Hansen & Grönvold, 2000). Glomerocrysts of olivine, augite, and plagioclase, which are close to textural equilibrium with the groundmass, are common in the tholeiites, indicating low-pressure, cotectic conditions during magma crystallisation (Jakobsson et al., 1978).

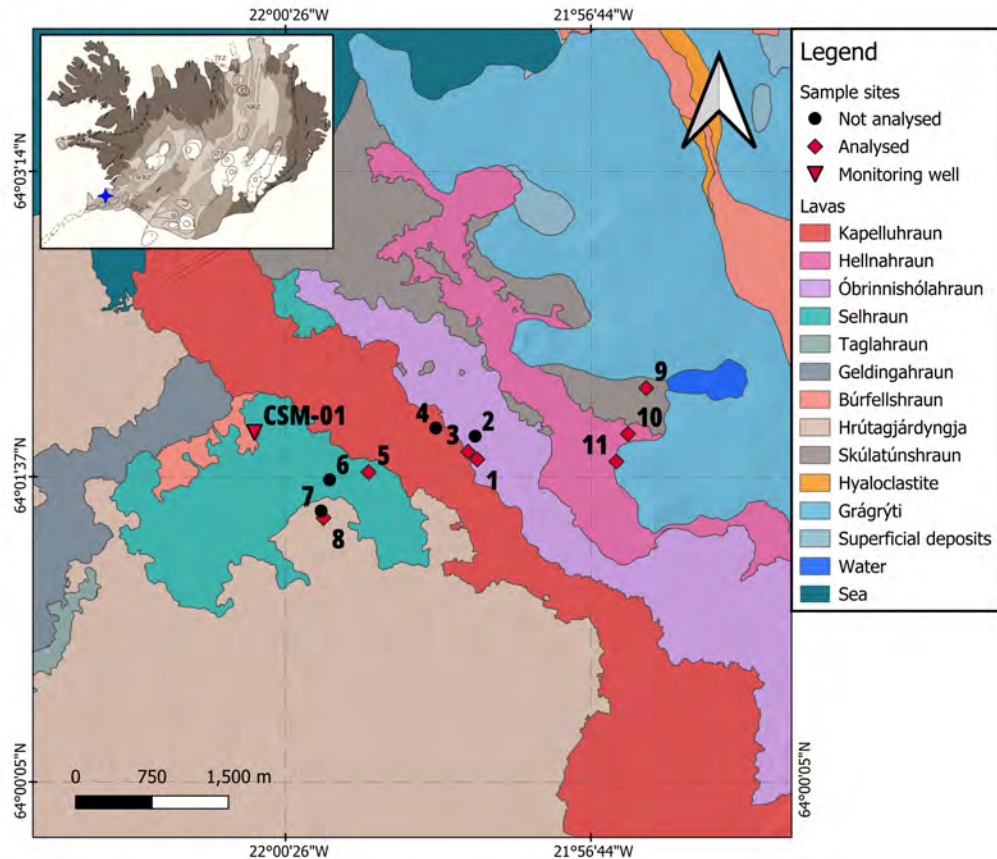


Figure 3: A map of the lavas in study area of the Straumsvík region ordered in chronological age from the top of the legend. The red triangle is the drill hole, the red diamonds are analysed sample sites, and black points are not analysed sample sites. The map is based on ÍSOR's geological map (Sæmundsson et al., 2010)

### 2.3 The Study Area

The Straumsvík Region is in the northern part of the Reykjavík Peninsula between the two volcanic systems, Svartsengi and Krýsuvík (see Figure 2). The area is characterised by mossy, broken-up pahoehoe lava fields relatively free of tectonic structures and minimal sources of seismicity in the area (Guðnason & Ágústsdóttir, 2023). The main source of the rock fields is from the Krýsuvík volcanic system. No source is local, and the lavas had to flow a relatively long distance to reach the area outside the zone of any of the six volcanic systems on the peninsula. The main source of lavas is coming from the Krýsuvík volcanic system. There are 8 lavas in the region: Kapelluhraun (1151 AD), Hellnahraun (950 AD), Óbrinnishólahraun (1900 to 2400 ka), Selhraun (2400 ka), Geldingahraun (4000 to 4500 ka), Búrfellshraun (7300 ka), Hrótagjárdyngja (7000 ka), and Skúlatúnshraun (7000 ka). Older lava is from earlier interstadials and is often called 'Grágrýti' due to its dull grey appearance (see Figure 3). These lavas are relatively young and can serve as a fresh baseline for comparison of the rock from monitoring well CSM-01 in this study.

## 3 Methods

### 3.1 Sample Collection

#### 3.1.1 Fieldwork

Fieldwork was conducted to collect representative rock samples from various lava formations in the Straumsvík area. The fieldwork was carried out over two days, in the fall of 2024, during which 14 rock samples were collected from eleven sample sites, of which seven were prepared and analysed from 6 different lava formations to represent an unaltered baseline of all analysed parameters (see Figure 4). Standard geological field equipment, including hammers, chisels, a notebook, a compass, a GPS-enabled phone (for photography and location recording), and sample bags, were used for sample collection and documentation. Field observations focused on describing the geological context of each site, including the relative position of each lava formation. For each sample, characteristics such as colour, grain coarseness, vesicularity, vesicle size, and the type and size of visible phenocrysts were documented. Notes were recorded in a field notebook, and photographs were taken to supplement descriptions and capture features of the formations. A geological map of the lavas was later made in QGIS with the locations of each sample in the area (“QGIS”, 2009). To see the coordinates of each sample, check Table S1 in the supplementary data.

#### 3.1.2 Monitoring well Cuttings Collection and Logging

Monitoring well CSM-01 was drilled to a total depth of 618 m (measured depth) and cased to 223 m. Cuttings were collected at 3 m intervals (6–603 m,  $n = 189$  samples). All samples were logged for stratigraphy, with volcanic rocks described for colour, grain size, phenocrysts, vesicularity (size and abundance), alteration minerals, and sample quality; sediment samples were noted for colour, grain size, and quality, with additional comments on any notable features. Given the petrological focus, detailed sediment analysis was limited to basaltic sands.

### 3.2 Sample Preparation

Preparation of 25 samples was done both for thin-section making and fusion into homogenised glass discs for X-ray fluorescence (XRF) analysis. These comprised 7 field samples and 18 well samples from Carbfix’s monitoring well CSM-01. The samples from the field were chosen to represent unaltered rock from six different basaltic lava formations which form the stratigraphy of the Straumsvík area. To represent the well’s stratigraphy, the 18 well samples were taken from depths of varying intervals. The primary criteria for selection was stratigraphic unit representation and sample quality. Grain size and alteration characteristics were considered to ensure samples represented the least altered geochemical composition of the basalts. The sample depth range was 18 m to 600 m. However, the distribution of selected samples within the monitoring well was predominantly from the anticipated permeable zone 318–372 m ( $n = 7$ ). Fewer

samples were obtained from the top 306 m ( $n = 7$ ) and the bottom 405 m to 600 m ( $n = 4$ ).

### 3.2.1 Thin-Section Preparation

Thin-sections were made from the same samples for petrographic description and mineral point counting. The samples were first cleaned and treated in ultrasonic baths (Bandelin Sonorex RK 100). The field samples were cut into rectangular blocks, 2 by 3.5 by 1.5 cm. Representative grains were selected from the well sample cuttings. The sample grains were placed on a sticky tape and then embedded in a standard petrographic epoxy resin in a circular shape with a 1.5 cm radius. The prepared samples were then sent to, Vancouver Petrographics (Canada), which made them into 30  $\mu\text{m}$  thick thin-sections.

### 3.2.2 Loss on ignition (LOI) and X-Ray fluorescence (XRF) Preparation

For the fusion into homogenised glass discs, samples were first cleaned and treated in ultrasonic baths (Bandelin Sonorex RK 100). Weathered surfaces were removed from field samples prior to powdering for geochemical analyses. Grains that did not represent the main lithology of each cutting depth were removed from cutting samples to be as close as possible to representing one stratigraphical unit. Samples were then crushed into small grains using a tungsten carbide jaw crusher (Retsch BB200) and further pulverised into powder using a tungsten carbide vibrating disc mill for 2 minutes (Retsch RS200). To lower the melting point of the samples, 5 g of flux (66% lithium tetraborate and 34% lithium metaborate) was mixed with 2 g of each sample and mixed thoroughly with a rod. The precision of each weighing was  $\pm 0.00002$  g (see Table S2 in the supplementary data). The powdered sample-flux mixtures were then placed in platinum crucibles and fused in an automated gas fusion machine, Phoenix VFD-4000 gas fusion machine by XRF Scientific, at 1100 °C. The machine allows for easily replicable, precise routines that eliminate any potential errors.

## 3.3 Analytical Techniques

### 3.3.1 Loss on Ignition (LOI)

Before the fusion of the sample powders, they were heated in an oven at 3 °C/min up to 1000 °C and held for 2 hours, then cooled to approximately 30 °C and loss on ignition (LOI) was determined. The powdered samples were weighed before and after heating using a Sartorius SECURA-1S microbalance with a precision of  $\pm 0.00001$  g and calculated as:

$$\text{LOI (wt.\%)} = \frac{100 \cdot (W_{C+S} - W_{1000^\circ\text{C}})}{W_{C+S} - W_C}$$

Where W stands for weight, C for crucible,  $W_{1000^\circ\text{C}}$  weight of crucible and sample after 1000 °C in the oven (see measurements in Table S3 in the supplementary data).

### 3.3.2 X-Ray Fluorescence Spectrometer (XRF)

For whole rock analysis, a Rigaku ZSX Primus II X-Ray Fluorescence Spectrometer (XRF) at the PetroTectonics analytical facility, Stockholm University, Sweden, was used. The concentrations of major elemental oxides ( $\text{SiO}_2$ ,  $\text{TiO}_2$ ,  $\text{Al}_2\text{O}_3$ ,  $\text{Fe}_2\text{O}_3$  (total),  $\text{MnO}$ ,  $\text{MgO}$ ,  $\text{CaO}$ ,  $\text{Na}_2\text{O}$ ,  $\text{K}_2\text{O}$ , and  $\text{P}_2\text{O}_5$ ) were determined in the prepared fused glass discs. The instrument is equipped with a thin beryllium window, a rhenium (Rh) X-ray tube, and a pentaerythritol tetranitrate (PET) crystal; it was calibrated using 24 known international standards. Matrix-matched USGS reference materials AGV-2 and BCR-2 were run every 10th sample to confirm analytical performance. Information regarding accuracy, precision, and detection limits is reported in the supplementary data Table S4. Calibration was performed using a series of international geological standards e.g., USGS rock standards BCR-2 for basalt, AGV-2 for andesite, and RGM-1 for rhyolite (see Table S4 in Supplementary data). Data reduction and matrix corrections were carried out using the standard software provided with the ZXS Primus II. The Rigaku ZSX Primus II measures total iron as  $\text{Fe}_2\text{O}_3$ . To determine the individual concentrations of  $\text{FeO}$  and  $\text{Fe}_2\text{O}_3$  a ratio of the ions' ratios needs to be assumed. The convention assumes that normal basalt contains  $\text{Fe}^{3+}$  ions at a ratio of 0.10 to total iron. The reported iron values in the results section are the calculated  $\text{FeO}$  and  $\text{Fe}_2\text{O}_3$  concentrations.

### 3.3.3 Cross, Iddings, Pirsson, Washington (CIPW) Norm Calculations

Cross, Iddings, Pirsson, and Washington (CIPW) norm calculation steps were performed after Johannsen, 1931 to determine normative mineral formations from the normalised whole-rock data, and an ion ratio of 0.1  $\text{Fe}^{3+}$  against total iron is assumed. This calculation provides an estimate of the ideal, normative mineralogy of a rock based on its bulk chemical composition. It is particularly useful for fine-grained or glassy rocks, such as the groundmass in these basalts, where optical mineral identification is difficult. Normative mineral data is reported in vol.% to complement point counting and expressed to one decimal place. Software written by Hollocher (2004) was used for calculations.

### 3.3.4 Point Counting

The Leica DMLSP polarising light microscope was used for both point counting and petrography. For the point counting, a stepping stage mounted on the microscope stage and SteppingStage Mk2 control box were utilised. The stepping stage was connected to a computer, and the software PetrogLite 5 was used to control the counting. A total of 500 points were counted in each sample. Based on each thin-section the area of point counting was defined; the well thin-sections were smaller in area than field sample thin-sections. A total of 6 categories were counted: plagioclase, pyroxene, olivine, groundmass, opaque oxides, and other alteration products. An attempt was made to count orthopyroxene, but due to microcrystallinity, identification was difficult. When identifiable, orthopyroxene was less than 1% of the area. Orthopyroxene was therefore

merged with clinopyroxene to form the pyroxene category. The attempt at counting glass was unsuccessful due to a lack of amorphous clear glass; it was therefore merged with the groundmass category. Errors were calculated as 2 standard deviations of the presented % of area according to Plas and Tobi (1965) (see Table S5 in Supplementary data).

### **3.3.5 Availability of Supplementary Data**

The supplementary data supporting the findings of this study are available as a separate file submitted alongside this thesis titled `Supplementary_data_DP.xlsx`. This file contains five tables (Tables S1-S5) detailing the full results of the analysis.

## 4 Results

The data for evaluating the abundance of reactive minerals and degrees of alteration in samples, which includes fresh field samples (PD-STV-24-...) and are compared with well cuttings from monitoring well CSM-01 (samples CSM-01-18m, -39m...). Unaltered reactive mineral phases are identified, and alteration is characterised on the basis of the results that will be presented as follows: lithology, petrography, geochemistry, normative calculations, and point counting.

### 4.1 Lithology

Fine- and medium-grained basaltic lavas are predominant in the stratigraphy of monitoring well CSM-01. Sediments and glassy basalts are commonly separating the formations. A single horizon of coarse-grained basalts is found. In total, seven sediment horizons interlayer the lava formations, 3-42 m thick, some containing shell fragments and often admixed with basalt. Alteration is generally minor. Oxidation, clay minerals, and silica were the main observed secondary phases, and below 400 m depth, zeolites were noted. Depths are reported in terms of the measured depth of the well.

#### 4.1.1 Lithology of Field Samples

Field samples were generally grey porphyritic, fine-grained basalts with plagioclase phenocrysts, and occasionally olivine phenocrysts were identified with moderate to significant vesicularity. PD-STV-24-01, seen in Fig. 4, had plagioclase (3 mm and 2% of area), very vesicular porphyritic basalt (7 mm and 30% of area), and no alterations. One sample, PD-STV-24-14, was coarse-grained, non-vesicular, with no phenocrysts and no alterations observed. The field samples all appear fresh in hand specimens.



Figure 4: Fresh surface of rock sample PD-STV-24-01, the sample shows high vesicularity and a few plagioclase phenocrysts (white specs within the grey mass). The hammerhead's length is 15 cm.

#### 4.1.2 Lithology of Monitoring Well CSM-01

##### **6–57 m: Fine-grained basalt**

This fine-grained grey basalt, sometimes medium-grained, is typically porphyritic. Vesicularity ranges from non-vesicular to highly vesicular (0.1-0.4 cm vesicles). Phenocrysts are mainly plagioclase (0.1-0.4 cm, 1-10% area) and olivine (0.1-0.4 cm, 1-7% area); pyroxene phenocrysts are rare. Plagioclase and olivine clusters up to 0.4 cm in size occur. Secondary minerals include clays and silica precipitations. Shell fragments, red grains, and mixed sedimentary/basaltic fragments occur notably at 39 m to 42 m. Mild to considerable oxidation is seen (levels 1-3). Mild clay alteration in vesicles and on fragments; some silica alteration occurs. Cuttings are missing at approximately 21-33 m.

##### **57–69 m: Sandstone**

Brownish-grey mix of rocks. This sandstone comprises fine-grained, dark brownish sand with shell grains, sandstone, and basalt fragments (60 m). At 63 m, the core primarily consists of fine sand with reddish rock fragments, shells, and some glassy or scoriaceous basaltic fragments.

##### **69–82 m: Missing cuttings**

Cuttings were not recovered. Ísor's drilling report notes circulation loss during drilling (Sigurgeirsson et al., 2024).

##### **82–86 m: Scoria**

Brownish-grey, primarily scoriaceous basalt fragments that can be reddish from oxidation, mixed with coarse sand with light brown grains and shell fragments.

##### **86–115 m: Medium-grained basalt**

Grey, medium-grained basalt containing plagioclase and abundant in olivine phenocrysts, and mildly oxidised.

##### **118–157 m: Sand**

Brownish-grey, fine- to medium-grained sand with some rounded basaltic gravel grains and larger light brown sediment grains. The gravel grains are mildly oxidised at several depths among the sediments.

##### **157–163 m: Medium-grained basalt**

Grey to brownish-grey, medium-grained basalt found at this depth.

##### **166–169 m: Sand**

Brown-grey, fine-grained sand and shell fragments are present.

##### **169–181 m: Medium-grained basalt**

Grey, medium-grained basalt containing olivine phenocrysts.

##### **181–187 m: Sand**

Brown-grey, medium- to coarse-grained sand. Shell grains are present, and clay is present in on top of sample at 187 m.

##### **190–223 m: Medium-grained basalt/oxidised Basalt**

Brown-grey to brown-red, medium-grained basalts. becoming moderately oxidised at 214-223 m. Light brown to faint green alteration clays are present in vesicles of basalts. Brown clay and shells at 223 m.

**225–227 m: Sand**

Brown-grey, medium-grained sand.

**227–240 m: Missing cuttings**

Cuttings were not recovered, possibly from the same unit as above.

**240–243 m: Scoria**

Dark red to light grey to moderately purple oxidised medium-grained basalt at 240 m with grey clay alteration accompanying. Very oxidised red scoria at 243 m; some grains are rounded.

**243–282 m: Coarse-grained Basalt**

Dark grey coarse-grained basalt reminiscent of sample PD-STV-24-14. Plag, olivine and pyroxene phenocrysts. The basalts are mildly oxidised at times. Brown mineral with metallic lustre is observed at 276 m.

**282–306 m: Medium-grained basalt**

Dark grey to dark red-purple, medium-grained basalts that show slight vesicularity. Plagioclase phenocrysts were found. considerably oxidised horizon at 297 m, possibly a scoria unit.

**306–327 m: Fine-grained basalt**

Grey to dark grey fine-grained basalts with moderate vesicularity. Glassy grains are found, and amygdules were observed in vesicles with green, pink, or beige alteration clays. Basalt shows mild to moderate oxidation of red grains at 318 m.

**327–330 m: Scoria**

Dark grey scoria, slightly vesicular and glassy; pistachio-green to white-filled vesicles with clay minerals.

**330–360 m: Fine-grained basalt**

Dark to light grey, fine-grained basalts. Slight vesicularity in some cases. Plagioclase (0.05 cm, 5%), olivine (0.05 cm, 1%) phenocrysts at 339 m. A green tint in the groundmass of 339 m could indicate a high amount of olivine in the groundmass. Some samples are very glassy amorphous silica needles (possibly formed post-sampling) at 357 m. Some vesicles contain amygdules of beige clay. Red grains at 350-351 m suggest some oxidation.

**360–372 m: Medium-grained basalt**

Dark grey, medium-grained basalt with gravelly cuttings and red grains are present showing moderate oxidation, flat and white to greyish mineral fragments are additionally seen.

**Depth Interval: 372–375 m: Glassy Basalt**

Dark grey glassy basalt is observed at this depth.

**Depth Interval: 375–400 m: Siltstone**

Dark grey to brown medium-grained siltstone. Light brown grains are observed at 382–384 m, with very fine sediment. Mostly dark, glassy grains at 390-393 m.

**400–408 m: Fine-grained basalt**

Dark grey, fine-grained basalt. Slightly vesicular at 405 m and glassy to fine-grained basalt with plagioclase phenocrysts noted at 405 m.

**408–420 m: Sandstone**

Brown-grey fine sandstone with sheared, flat cuttings. Red, light grey, brown, and light grey-green clay grains are observed. Flat grains of brown fine sediments showing layering and slight oxidation of scoria is mixed in with the sediments.

**420–471 m: Fine-grained basalt/Cement**

Grey to brown-grey fine-grained basalt, olivine and plagioclase porphyritic. Red grains of mild oxidation are observed. Light beige and light green grains are seen, and possibly red chalcedony. A cement unit is noted at 444 m.

**471–474 m: Scoria**

grey vesicular scoria is at a depth of 471 m to 474 m.

**474–513 m: Fine-grained basalt**

Light grey to grey fine-grained basalt which are composed of crushed olivine and Plag. It is tough to identify any texture in the basalt. Greenish tint hinting at olivine abundance. Mild to moderate oxidation is observed at 483 m, 489 m, and 498 m.

**513–528 m: Mix of Basalt and Sediments**

Reddish-brown mix of fine-grained basalt and sediments. Sheared flat grain cuttings of sedimentary layers. The basalt shows a mild to moderate oxidation.

**528–537 m: Medium-grained basalt**

Light grey, medium-grained basalt with mild oxidation of red grains at 534 m depth.

**537–540 m: Scoria**

Moderately oxidised reddish-brown scoria.

**540–546 m: Medium-grained basalt**

Brown-grey, medium-grained basalt mildly oxidised, exhibiting few red grains at 540 m depth.

**546–561 m: Mix of Basalt and Sediments**

grey-brown mix of basalt and sediments. The grains are variously coloured: pink-red, light grey, light brown sandy sediments admixed and light grey sheared flat grains. Angular dark grey basalt grains (0.5 cm) are seen at 558 m depth. Dark purple grains of basalt show mild to moderate oxidation.

**561–570 m: Medium-grained basalt**

Light grey, medium-grained basalt. White needle-like precipitates at 567 m depth and amorphous silica is observed.

**570–573 m: Scoria**

Moderately oxidised reddish-brown to grey scoria.

**573–603 m: Fine-grained basalt**

Dark grey to dark red-grey fine-grained basalt. Grey-brownish glassy grains were observed. Light grey clay at 600 m. Mild oxidation is observed at depths of 573 m to 579 m. Minor clay, amorphous silica, and thomsonite were observed in the lower part.

Field and well samples both were predominantly porphyritic fine- to medium-grained basalts, and both had coarse-grained basalt (PD-STV-24-14 and depth 243-282 m) (see Fig. 5). Monitoring well CSM-01 had an alteration, mainly of oxidation that progressed with depth and is shown in Fig. 5 from none, mild, and moderate to (0-3). In parallel,

clays and zeolites were noted at depths below 400 m. While field samples showed no alterations in hand specimens.

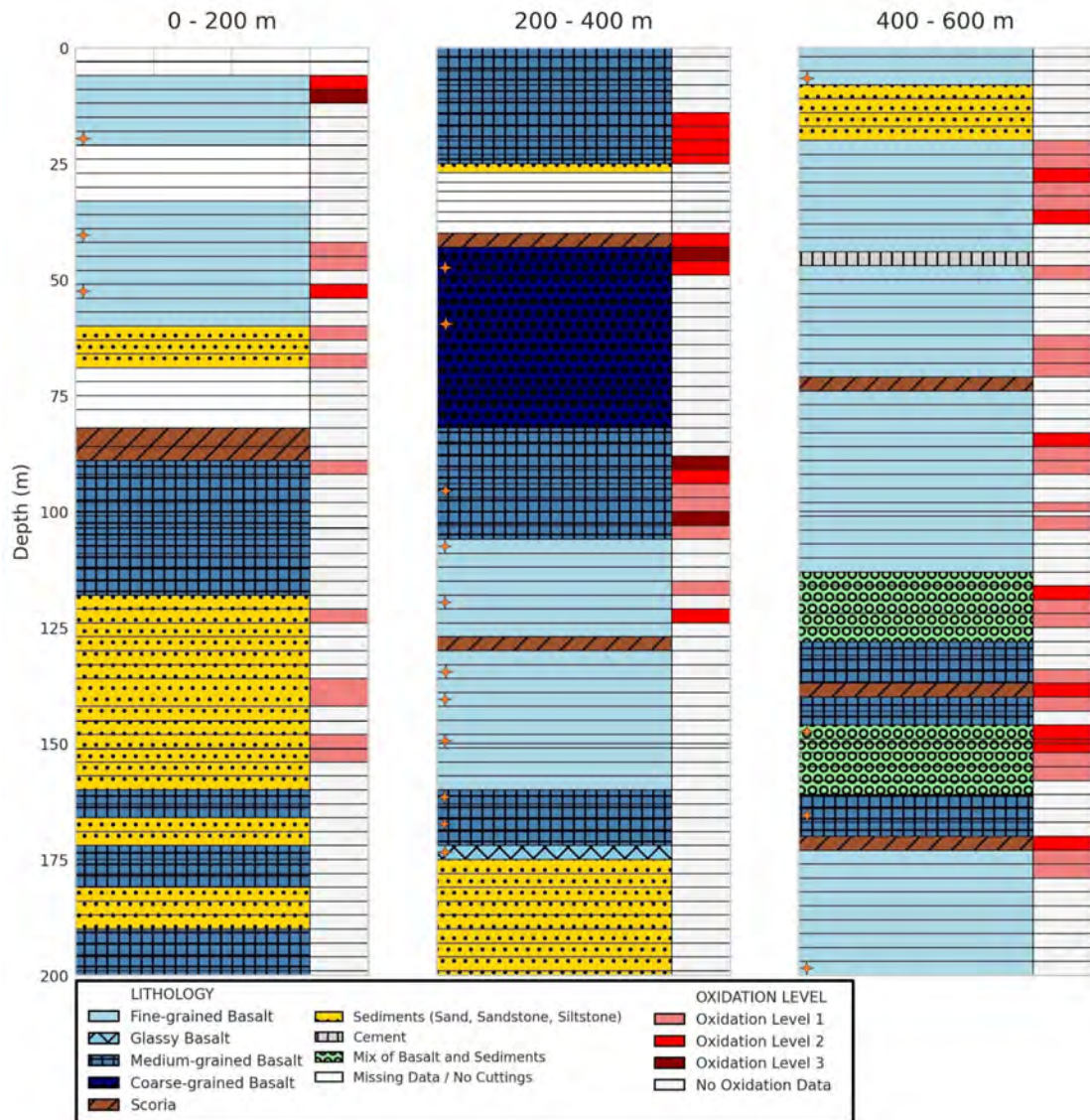


Figure 5: Log of monitoring well CSM-01, represented in three columns: topmost 200 m on the left, 200-400 m in the middle, and on the right 400-600 m. Every cell represents 3 m of depth. Orange stars represent where samples were analysed. Oxidation levels are represented by colours: level 0 as white (none), level 1 as light red (mild), level 2 as red (moderate), and level 3 as dark red (considerable).

## 4.2 Petrography

Petrographic analysis shows a consistent porphyritic tholeiitic basaltic mineralogical assemblage of plagioclase, olivine, pyroxene (orthopyroxene and clinopyroxene), and oxides. Fine-grained groundmass filled in the spaces between phenocrysts and is often dominant. The general textures of samples are hypocrySTALLINE, with intersertal devitrified glass to intergranular fine groundmass (20-50  $\mu\text{m}$ ), mostly composed of plagioclase

and clinopyroxene phenocrysts. These samples are most often subhedral and are between 500 and 1500  $\mu\text{m}$  in size and occasionally display ophitic texture. Generally, plagioclase is the dominant primary mineral and occurs as subhedral to euhedral phenocrysts and acicular or elongated microlites. Plagioclase has low relief and has first-order interference colours in cross-polarised light (XP). Olivine is typically found as subhedral phenocrysts, often equant or slightly elongate with typical fractures. It occurs as interstitial microlites, but not commonly. Olivine displays high relief and bright second- to third-order interference colours in XP. Clinopyroxene is mostly subhedral, forming interstitial microlites or small microphenocrysts with moderate relief and interference colours up to high second order. The dark groundmass suggests devitrification of the glass with plagioclase needles. Alteration is generally limited but variably developed across the samples, depending on suites, but from fresh to moderate alteration with depth.

The samples represent three petrographic suites: porphyritic glassy basalts with hyalopilitic texture, porphyritic intergranular basalt containing some degree of cryptocrystalline glassy groundmass, and coarse porphyritic basalt containing megacrysts (500–1000  $\mu\text{m}$ ) and almost no glassy groundmass. The first suite corresponds to scoria, glassy, and fine-grained basalt (see Section 4.1) and contains 6 samples (CSM-01-39m, -333m, -372m, -546m, -600m, PD-STV-24-11). The second suite is fine- to medium-grained basalts containing 11 samples (CSM-01-18m, -51m, -306m, -318m, -339m, -348m, -405m, -564m, PD-STV-24-01, -03, and -05). And the third to medium- to coarse-grained basalts containing 8 samples (CSM-01-246m, -258m, -294m, -360m, -366m, PD-STV-24-08, -09, and -14). The samples show minimal alteration in the top 372 m, and oxidation of grains is the most common alteration. The alteration becomes more prevalent in the deeper samples (405–600 m), showing formations of clays, zeolites, calcite, and oxides. Samples CSM-01-405m, -546m, -564m, and -600m showed a variety of grain sizes in the samples and are assumed to represent more than one lava formation, but their most abundant grain-size grains determined their suite. They are still kept a part of the results but kept in mind while discussed.

#### 4.2.1 Porphyritic Glassy Basalt

Basalts in this suite exhibit textures of porphyritic intersertal groundmass. Plagioclase often has elongated laths (100  $\mu\text{m}$  to 600  $\mu\text{m}$ ) with albite twinning. Olivine phenocrysts are from 100 to 300  $\mu\text{m}$ . The pyroxenes are subhedral and range from 90 to 400  $\mu\text{m}$  in phenocryst size. As seen in the sample PD-STV-24-11 devitrified glass, hyalopilitic texture with acicular plagioclase and clinopyroxene in brown and dark purple (Fig. 6). CSM-01-39m is the only sample not devitrified and shows a brown glassy texture in the groundmass with hyalopilitic features of acicular and skeletal plagioclase microlites in the glassy groundmass. It also contains glomerocrysts with white to grey equal subhedral plagioclase. The preservation of primary phases is generally good in this suite. Plagioclase is fresh, having incipient alteration, such as minor fracturing, or resorption and recrystallisation indicated (see CSM-01-372m in Fig. 6). Olivine is often

subhedral and fractured but shows no significant alteration. Clinopyroxenes sometimes show blotched chemical zoning (see CSM-01-600m in Fig. 6).

Secondary minerals include brownish clay minerals and show most often on borders of grains with low birefringence, fibrous, or void-filling phases in CSM-01-546m. Oxides are found in these samples and are anhedral to subhedral (50-100  $\mu\text{m}$ ).

Dissolution can contribute to vuggy porosity subsequently filled by secondary minerals, especially in more altered samples (e.g., CSM-01-546m). Fine-grained secondary oxides and clay minerals are also disseminated within the groundmass.

Sample CSM-01-39m (glassy basalt) shows incipient to weak alteration, primarily minor alteration of its glassy groundmass but relatively fresh plagioclase. Samples CSM-01-318m, CSM-01-333m, CSM-01-372m, and CSM-01-600m exhibit weak alteration. The most altered sample of this suite, CSM-01-546m, shows relatively moderate alteration, where secondary minerals are predominantly clays and possibly zeolites. Consequently, the proportion of primary minerals ranges from >99% in the freshest glassy basalts to >95% recognisable primary minerals in CSM-01-546m.

The CSM-01 cuttings demonstrate alteration from incipient devitrification and minor groundmass alteration to the appearance of secondary phases such as clays, iron oxides, and minor zeolite formation of thomsonite.

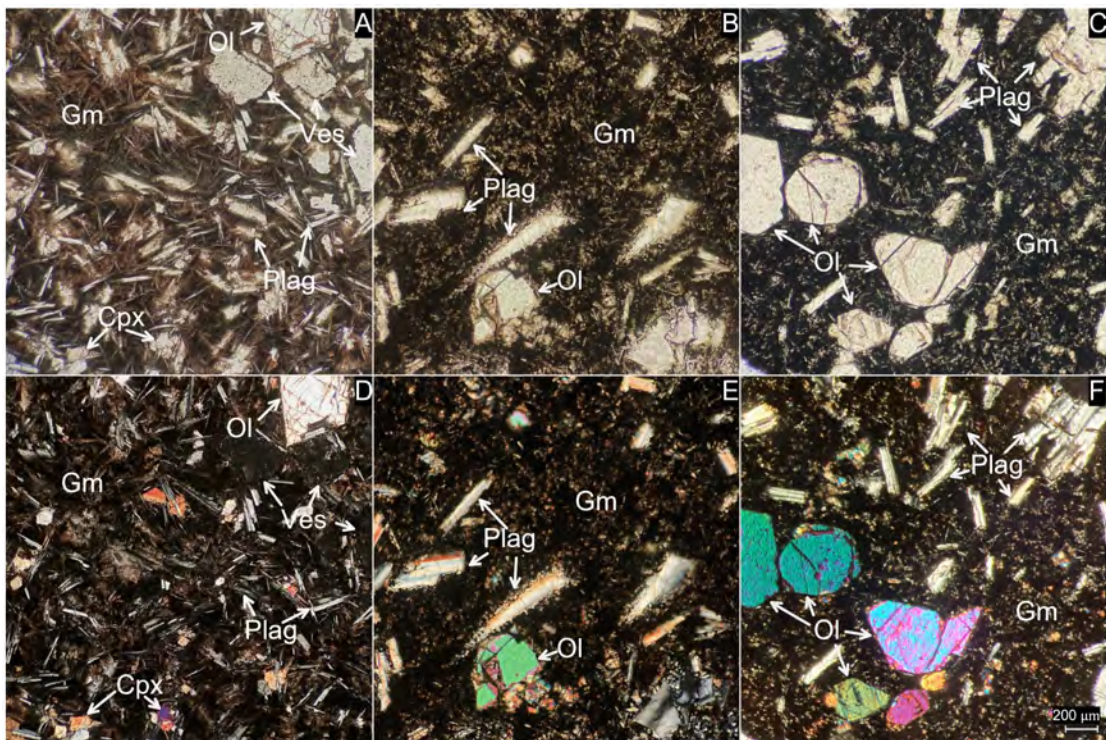


Figure 6: A, B, and C are PP, and D, E, and F are XP. Micrographs A and D show sample PD-STV-24-11. Micrographs B and E show sample CSM-01-372m. Micrographs C and F show sample CSM-01-600m. Abbreviations: Plag: plagioclase, Ol: olivine, Cpx: clinopyroxene, Ox: opaque oxides, Gm: groundmass, Ves: vesicle, Alt: alteration. The scale line (200  $\mu\text{m}$ ) applies to all micrographs.

### 4.2.2 Porphyritic Intergranular Basalt

These fine- to medium-grained intergranular basalts typically exhibit a porphyritic to seriate texture, with phenocrysts and microphenocrysts of plagioclase (100–800  $\mu\text{m}$ ), clinopyroxene (100–300  $\mu\text{m}$ ), and olivine (150–350  $\mu\text{m}$ ) set within a finer-grained intergranular groundmass (20–50  $\mu\text{m}$ ) (see Fig. 7).

Plagioclase occurs as euhedral to subhedral, elongate laths showing characteristic albite twinning, and zoning within twins is common; observed devitrified glass is around 10%. Pyroxenes are generally subhedral, equant to prismatic, and interstitial clinopyroxene are the bulk of pxs observed. Olivine, when fresh, forms euhedral to subhedral, often equant crystals, though it is frequently altered by oxidation. Inclusions of opaque microlites showing cubic crystal habit (5–15  $\mu\text{m}$ ) in both the plagioclase and olivine are common. The groundmass is made up of 20–50  $\mu\text{m}$  clinopyroxene and orthopyroxene (40% of area) and sporadic olivine grains (>5%) and 50–100  $\mu\text{m}$  elongated plagioclase microlites 20–80  $\mu\text{m}$  (45%) and disseminated anhedral to subhedral opaque Fe-Ti oxides (50–150  $\mu\text{m}$ ) (see Fig. 7). The groundmass can have patches of cryptocrystalline glass (10 to 20% of the groundmass) in the more commonly fine-grained intergranular texture (50–60% of total area) against phenocrysts.

Alteration is variably developed across the suite, generally increasing with depth, with common secondary minerals including brownish to opaque in PP. CSM-01-339m exhibited vein alteration into Idd and brown clay along fractures, one leading to an olivine that is pseudomorphed to Idd. More cryptocrystalline to fine-grained clay mineral patches of iddingsite (500  $\mu\text{m}$ ) (see CSM-01-348m in Fig. 7). Primary minerals range from fresh to showing incipient alteration like minor fracturing, zoning, and/or resorption to pervasive brown to opaque (PP) clay or iddingsite replacement of plagioclase (20–30% of crystal) and olivine (10–20%) (see CSM-01-348m in Fig. 7). Oxides are seen subhedral around olivine and pyroxene phenocrysts. With more depth the colour of devitrified opaque cryptocrystalline glass becomes less fuzzy and more blocky, altered to oxide.

### 4.2.3 Medium- to Coarse-grained Basalt

The basalts in this suite are coarser-grained and hypo- to holocrystalline, predominantly exhibiting an intergranular texture (see Fig. 8). The biggest difference between the fine-grained intergranular basalt and coarser-grained basalt is that there is a significant difference between the proportionality of groundmass against phenocrysts. In the fine-grained intergranular basalt the groundmass can be from 50% to 70% while in the coarse-grained basalt the groundmass is less than 10% to 40%. This texture is characterised by a framework of relatively coarse plagioclase laths (300–800  $\mu\text{m}$ ) with interstitial clinopyroxene (150–400  $\mu\text{m}$ ) and opaque oxides (50–300  $\mu\text{m}$ ). Some samples also display porphyritic textures (e.g., CSM-01-360m, CSM-01-366m, PD-STV-24-08) of olivine and px grains with distinct phenocrysts of plagioclase and olivine set within intergranular groundmass, while others show subophitic textures in olivine, e.g., CSM-01-258m, PD-STV-24-09, PD-STV-24-14 (see PD-STV-24-14 in Fig. 8).

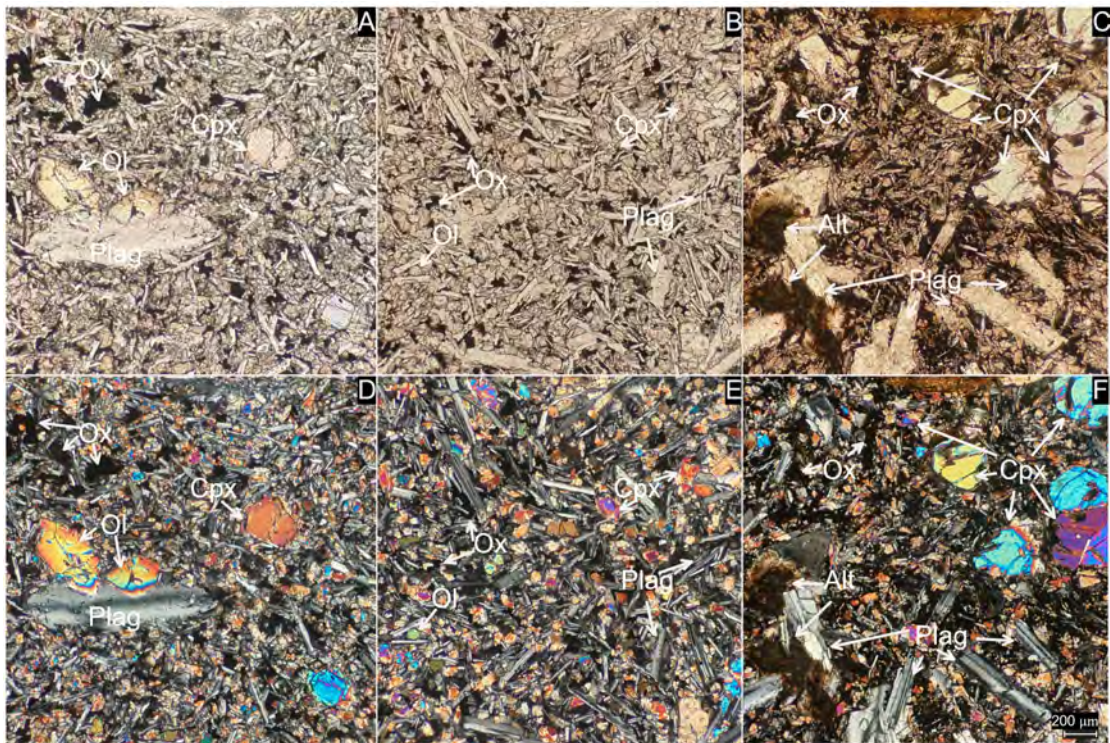


Figure 7: A, B, and C are PP, and D, E, and F are XP. Micrographs A and D show sample PD-STV-24-03. Micrographs B and E show sample CSM-01-51m. Micrographs C and F show sample CSM-01-348m. Abbreviations: Plag: plagioclase, Ol: olivine, Cpx: clinopyroxene, Ox: opaque oxides, Alt: alteration. The scale line (200  $\mu\text{m}$ ) applies to all micrographs.

Plagioclase occurs as euhedral to subhedral, elongate laths and as larger, often tabular (see CSM-01-258m in Fig. 8) but more elongated in field samples, displaying characteristic first-order grey to white birefringence and albite twinning. Clinopyroxene is present mainly as subhedral to anhedral interstitial grains, but larger subhedral phenocrysts are found; faint purplish colour is suggestive of titanaugite; it shows moderate relief and interference colours typically ranging from upper first to mid-second order. Opxs are found as interstitial grains but are less common and difficult to recognise from clinopyroxene interstitial grains due to size. Olivine generally occurs as subhedral large phenocrysts (larger than 500  $\mu\text{m}$ ), often equant or slightly elongate; fresh olivine (e.g., cores in PD-STV-24-09). Embayment of olivine phenocrysts is observed; inclusions of magnetite are additionally seen. The groundmass (30–80  $\mu\text{m}$ ) is predominantly holocrystalline intergranular, though the "hypocrystalline" nature of some rocks in the suite suggests variability in the degree of crystallinity of the finest interstitial material or the presence of minor glass in some instances, therefore indicating a seriated texture. Opaque oxides, likely titanomagnetite or ilmenite, are ubiquitously disseminated as anhedral to subhedral grains within the groundmass interstices or as minor inclusions in phenocrysts. In CSM-01-258m multitude of subhedral magnetite with sieve texture is found (800  $\mu\text{m}$ ).

Similarly to the earlier described suites, alteration is variably developed across the suite, generally increasing with depth, with common secondary minerals including brownish to opaque in PP iddingsite (500  $\mu\text{m}$ ) (see CSM-01-294m in Fig. 8). All primary minerals show some amount of zoning. Plagioclase is often zoned, showing grey to brown interference colours with albite twins and sometimes reaction rims, possibly smectite, as seen in CSM-01-294m in Fig. 8. In CSM-01-366m both plagioclase (600  $\mu\text{m}$ ) and olivine (150  $\mu\text{m}$ ) are found pseudomorphed by calcite in high iridescent interference colours. partially in the olivine (30% of grain) and the plagioclase wholly. Olivine are often altered by oxidation, surrounded by opaque oxides and showing red colours of haematite and iddingsite, with the most pervasive in sample CSM-01-294m in Fig. 8. Clinopyroxenes are often found zoned in a blotched nature. Olivine when found as interstitial grains in the porphyritic samples of this suite (CSM-01-360m, CSM-01-366m, PD-STV-24-08), exhibited rainbow-like propagating colours of high interference colours. In sample CSM-01-366m, a brown secondary clay mineral both in PP and XP fills a pore, with zoned reaction rims outlining the pore. The texture of the mineral is fibrous and is accompanied by anhedral magnetite. These prominently include clay minerals (appearing as fine-grained brownish, greenish, or greyish aggregates (size) with low birefringence, likely smectite) and iron oxides/hydroxides (reddish-brown, orange, or opaque phases (size) such as iddingsite, goethite, or haematite).

### 4.3 Geochemistry

Results of major elemental geochemistry is described in the context of carbon sequestration. The rocks exhibit high CaO (11.14-13.55 wt.%), FeO (7.76-12.66 wt.%), and MgO (7.62-10.40 wt.%). Geochemical classification is made using total alkali silica (TAS)

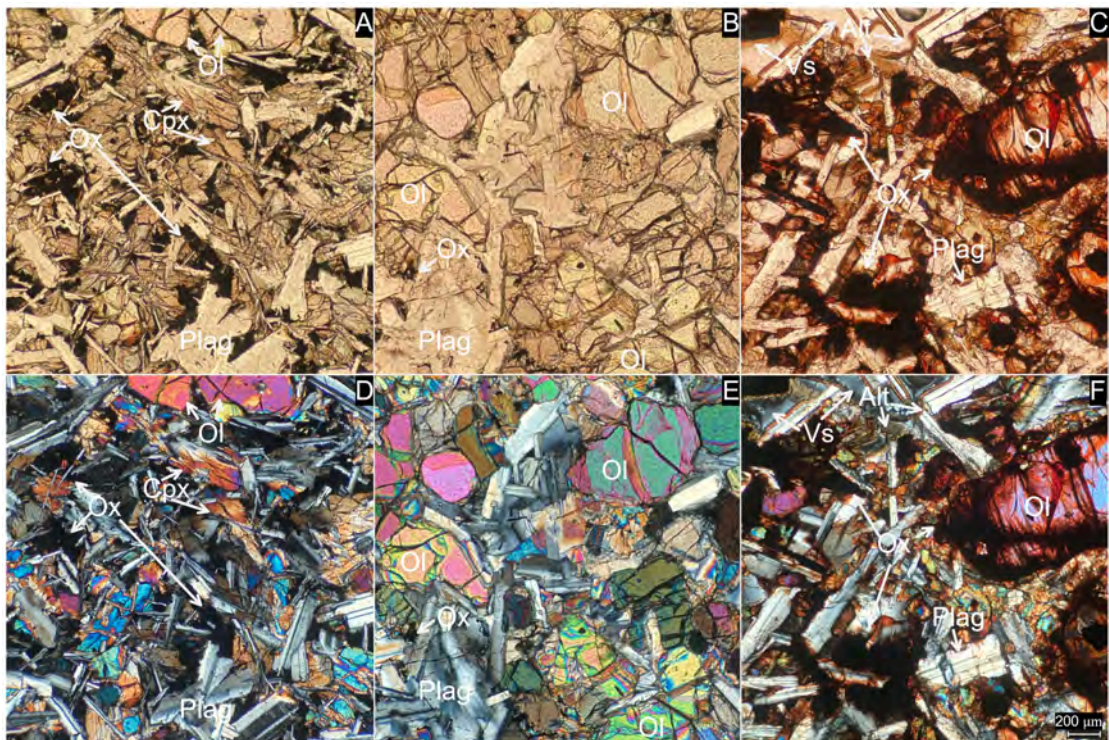


Figure 8: A, B, and C are PP, and D, E, and F are XP. Micrographs A and D show sample PD-STV-24-14. Micrographs B and E show sample CSM-01-258m. Micrographs C and F show sample CSM-01-294m. Abbreviations: Plag: plagioclase, Ol: olivine, Cpx: clinopyroxene, Ox: opaque oxides, Vs: vesicle, Alt: alteration. The scale line (200  $\mu\text{m}$ ) applies to all micrographs.

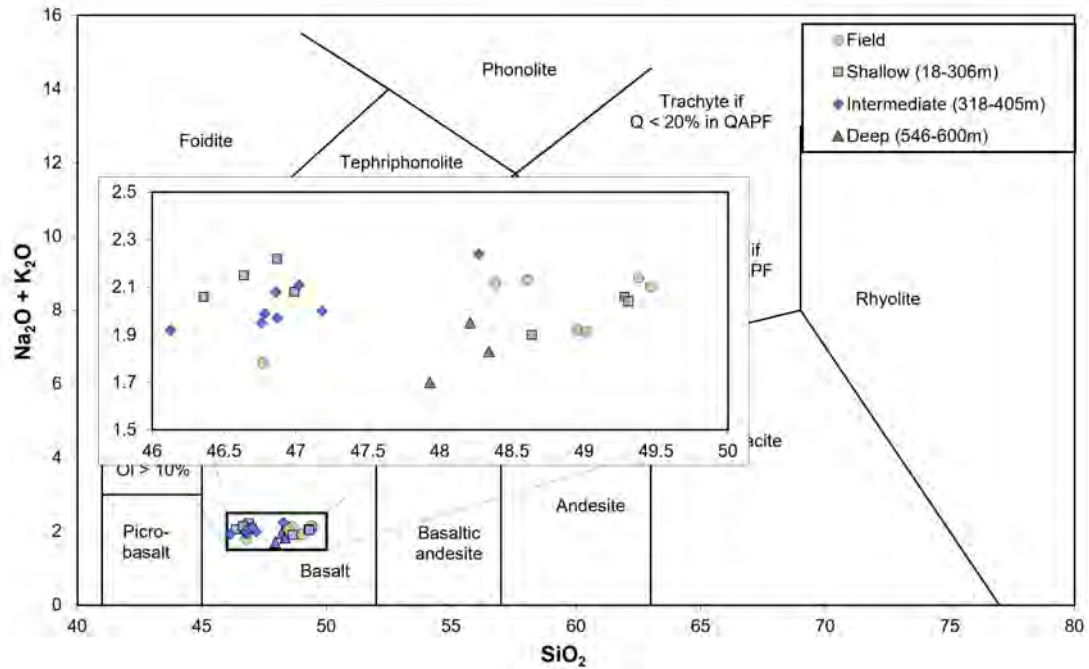


Figure 9: TAS (wt. %) diagram of the field samples in light green circles, and the samples from monitoring well CSM-01, with shallow (18-306 m) samples as light blue squares, intermediate depth samples (318-405 m) as blue diamonds, and deep-well samples (546-600 m) as purple triangles (Le Bas et al., 1986).

and alkali-iron-magnesium (AFM) (Figs. 9 and 10). Variations in major oxide concentrations with increasing MgO content are presented (Fig. 11). Loss on Ignition (LOI) values are then presented with depth in Fig. 12.

#### 4.3.1 Total Alkali Silica (TAS) Classification

On a total alkali-silica (TAS) Fig. 9, all the whole-rock data demonstrates that analysed samples classify as basalt. These samples exhibit a relatively restricted range in silica content, varying from 46.1-49.5 wt.%  $\text{SiO}_2$ . Correspondingly, total alkali contents ( $\text{Na}_2\text{O} + \text{K}_2\text{O}$ ) range from 1.6-2.3 wt. %, as magnified in the inset figure, showing bimodal clusters split by 47.5% .

Samples from the field (STV-FS) display  $\text{SiO}_2$  values between approximately 48.3 wt. % and 49.5 wt. %, with total alkalis from 1.8 wt.% to 2.2 wt.%. The shallow drill-hole samples (CSM-01) show  $\text{SiO}_2$  ranging from approximately 46.3 wt.% to 49.5 wt.% and total alkalis from 1.9 wt.% to 2.2 wt.%. Intermediate drill-hole samples plot with  $\text{SiO}_2$  contents between approximately 46.1 wt.% and 47.2 wt.% and total alkalis from 1.9 wt.% to 2.2 wt.%. The deep-well samples exhibit  $\text{SiO}_2$  values from approximately 47.9 wt.% to 48.5 wt.% and are characterised by the lowest total alkali contents among the groups, ranging from approximately 1.6 wt.% to 1.9 wt.%. Despite these subtle variations, particularly the slightly lower alkali content in the deep-well samples, all units consistently fall within the basalt classification field.

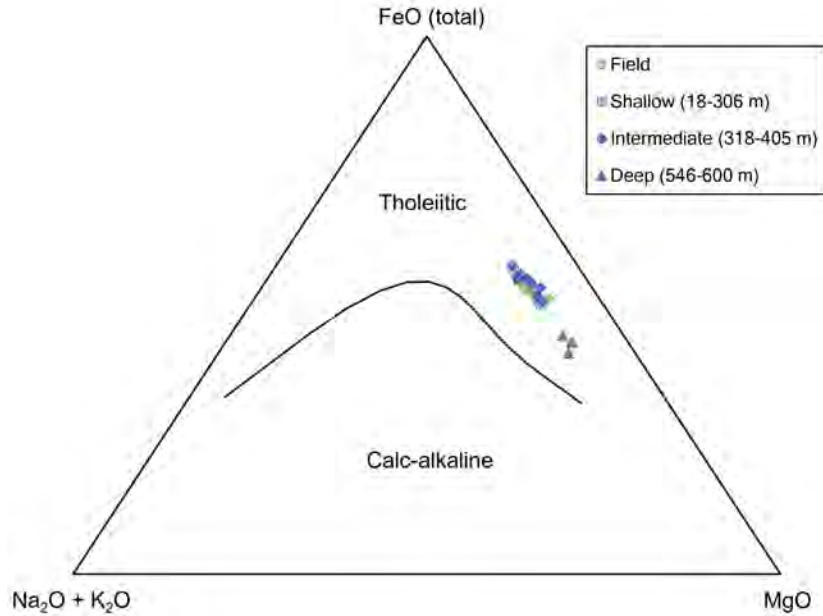


Figure 10: AFM ( $\text{Na}_2\text{O} + \text{K}_2\text{O}$ ,  $\text{FeO}_{\text{total}}$ , and  $\text{MgO}$ , all in wt.%) diagram illustrating the tholeiitic affinity of the analysed samples. The dividing line between tholeiitic and calc-alkaline fields is after Vermeesch and Pease (2021). Symbols represent field samples (light green circles), shallow well cuttings (18-306 m; light blue squares), intermediate well cuttings (318-405 m; Blue diamonds), and deep-well cuttings (546-600 m; purple triangles).

#### 4.3.2 Alkali Iron Magnesium Diagram (AFM)

The TAS diagram (Fig. 9) shows the samples are sub-alkaline. The AFM ternary diagram (Fig. 10) further distinguishes between tholeiitic and calc-alkaline magma series. All samples, including field samples (light green circles), shallow well cuttings (18-306 m; light blue squares), intermediate well cuttings (318-405 m; blue diamonds), and deep well cuttings (546-600 m; purple triangles), plot unequivocally within the tholeiitic field, following a trend of iron enrichment relative to magnesium, with a relatively low alkali component. Specifically, the field samples, shallow well cuttings, and intermediate well cuttings form a concentrated group showing this iron enrichment. The deep well cuttings also fall within the tholeiitic field but are displaced towards the  $\text{MgO}$  apex and slightly away from the  $\text{FeO}_{\text{total}}$  apex compared to the other groups, indicating a higher relative proportion of magnesium.

#### 4.3.3 $\text{MgO}$ against Oxides

The major element variations relative to  $\text{MgO}$  content are presented in Fig. 11. Overall, the samples range from  $\sim 7.6$  to  $\sim 10.4$  wt.%. The field samples  $\text{MgO}$  contents ranged from  $\sim 7.7$  to  $\sim 8.4$  wt.%. Shallow-well samples (18-306 m) display  $\text{MgO}$  contents in a range of  $\sim 7.6$  to 9.9 wt.%. Mid-well samples (318-405 m) range from  $\sim 7.6$  to  $\sim 10.3$  wt.% in  $\text{MgO}$  content. The deep-well samples (546-600 m; pink triangles) are characterised by the highest  $\text{MgO}$  contents, with  $\sim 10.0$  to  $\sim 10.4$  wt.%.

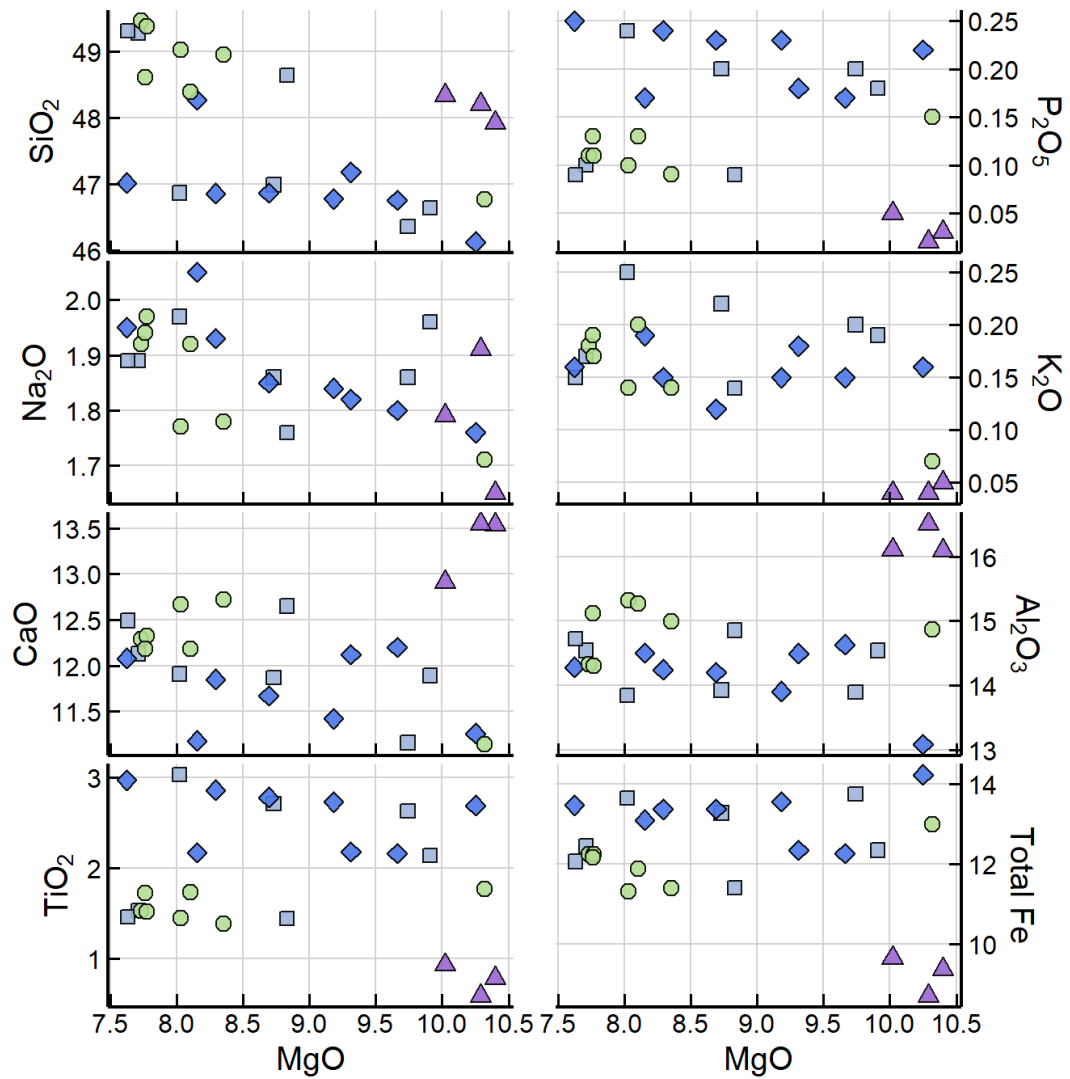


Figure 11: Harker diagrams with MgO (wt.%) on x-axis and in the left column of SiO<sub>2</sub>, Na<sub>2</sub>O, CaO, and TiO<sub>2</sub> (all in wt.%) in y-axis. In the right column, P<sub>2</sub>O<sub>5</sub>, K<sub>2</sub>O, Al<sub>2</sub>O<sub>3</sub>, and total Fe (sum of FeO and Fe<sub>2</sub>O<sub>3</sub>, wt.%). Samples are differentiated by depth and correspond to field samples (light green circles), shallow well samples (18-306 m; light blue squares), intermediate well samples (318-405 m; blue diamonds), and deep well samples (546-600 m; purple triangles).

The field samples all cluster within a relatively low MgO content and SiO<sub>2</sub> content, apart from one sample (PD-STV-24-14), which plots with relatively high MgO content and low SiO<sub>2</sub> content. The shallow and intermediate well samples show a general negative correlation with MgO. Furthermore, the top-depth well samples (within the shallow depth samples) of 18 m, 39 m, and 51 m plot within the cluster of the field samples with low MgO content and high SiO<sub>2</sub>. Intermediate well samples, also indicating a scattered negative trend. Deep-well samples plot in a cluster of high MgO and SiO<sub>2</sub> content.

The samples range from  $\sim 0.09$  to  $\sim 0.25$  wt.% in P<sub>2</sub>O<sub>5</sub>. They cluster at low MgO and low P<sub>2</sub>O<sub>5</sub> with the exception of PD-STV-24-14. The shallow samples from 246-306 m and the intermediate well samples show a negative correlation trend, while the topmost shallow well samples (18-51 m) cluster with the field samples as well as the CSM-01-405m sample. The deep-well samples cluster in high magnesium and low P<sub>2</sub>O<sub>5</sub>  $\sim 0.02$  to  $\sim 0.05$  wt.%. The samples range from  $\sim 1.7$  to  $\sim 2.20$  Na<sub>2</sub>O content. The shallow-well samples range from  $\sim 1.75$  to  $\sim 2.00$ . The intermediate well samples range from  $\sim 1.76$  to  $\sim 2.20$  in wt.%, and the deep-well samples show a range of  $\sim 1.68$  to  $\sim 1.91$  wt.%. Together, they all show a negative trend with the MgO.

In the K<sub>2</sub>O plot, the range of field samples is from  $\sim 0.07$  to  $\sim 0.2$  wt.%. The shallow well samples are from  $\sim 0.14$  to  $\sim 0.25$  wt.%. The intermediate samples range from  $\sim 0.12$  to  $\sim 0.19$  wt.% and the deep-well samples plot with very low concentrations of  $\sim 0.04$  to  $\sim 0.05$  wt.%. The deep-well samples and PD-STV-24-14 cluster together with high MgO and low K<sub>2</sub>O, while the rest of the samples have a horizontal correlation.

Calcium oxide (CaO) concentrations vary from  $\sim 11.2$  to  $\sim 13.5$  wt.%. A general negative correlation between CaO and MgO is observed for the field, shallow-, and mid-well samples, with CaO decreasing from  $\sim 12.8$  wt.% to  $\sim 11.2$  wt.% with increasing MgO. Similar to Al<sub>2</sub>O<sub>3</sub>, the deep-well samples display two CaO clusters at high MgO: one with lower CaO ( $\sim 11.4$  wt.% and  $11.6$  wt.%) and another with higher CaO ( $\sim 12.9$  wt.% and  $13.2$  wt.%).

Alumina (Al<sub>2</sub>O<sub>3</sub>) contents range from approximately  $13.1$  wt.% to  $16.5$  wt.%. Field, shallow-, and mid-well samples show a negative correlation between Al<sub>2</sub>O<sub>3</sub> and MgO, with Al<sub>2</sub>O<sub>3</sub> decreasing from  $\sim 15.5$  wt.% down to  $\sim 13.9$  wt.% as MgO increases from  $\sim 7.5$  wt.% to  $\sim 10.2$  wt.%. The deep-well samples exhibit two distinct Al<sub>2</sub>O<sub>3</sub> clusters at their high MgO range: one group with lower Al<sub>2</sub>O<sub>3</sub> ( $\sim 13.2$  wt.% and  $13.7$  wt.%) and another with markedly higher Al<sub>2</sub>O<sub>3</sub> ( $\sim 16.0$  wt.% and  $16.5$  wt.%).

TiO<sub>2</sub> concentrations range from approximately  $0.5$  wt.% to  $3.0$  wt.%. Surface, shallow, and mid-well samples exhibit a clear negative correlation between TiO<sub>2</sub> and MgO, with TiO<sub>2</sub> increasing from as low as  $\sim 1.2$  wt.% up to  $\sim 3.0$  wt.% as MgO decreases from  $\sim 10.2$  wt.% to  $\sim 7.5$  wt.%. The deep-well samples are notably depleted in TiO<sub>2</sub>, with all four samples showing low values between  $\sim 0.5$  wt.% and  $1.0$  wt.% at their high MgO contents.

All samples exhibit high concentrations of divalent cations, consistently exceeding  $30$  wt.%. The measured concentrations range from  $30.76$  wt.% (sample PD-STV-24-08) to  $33.13$  wt.% (sample CSM-01-258).

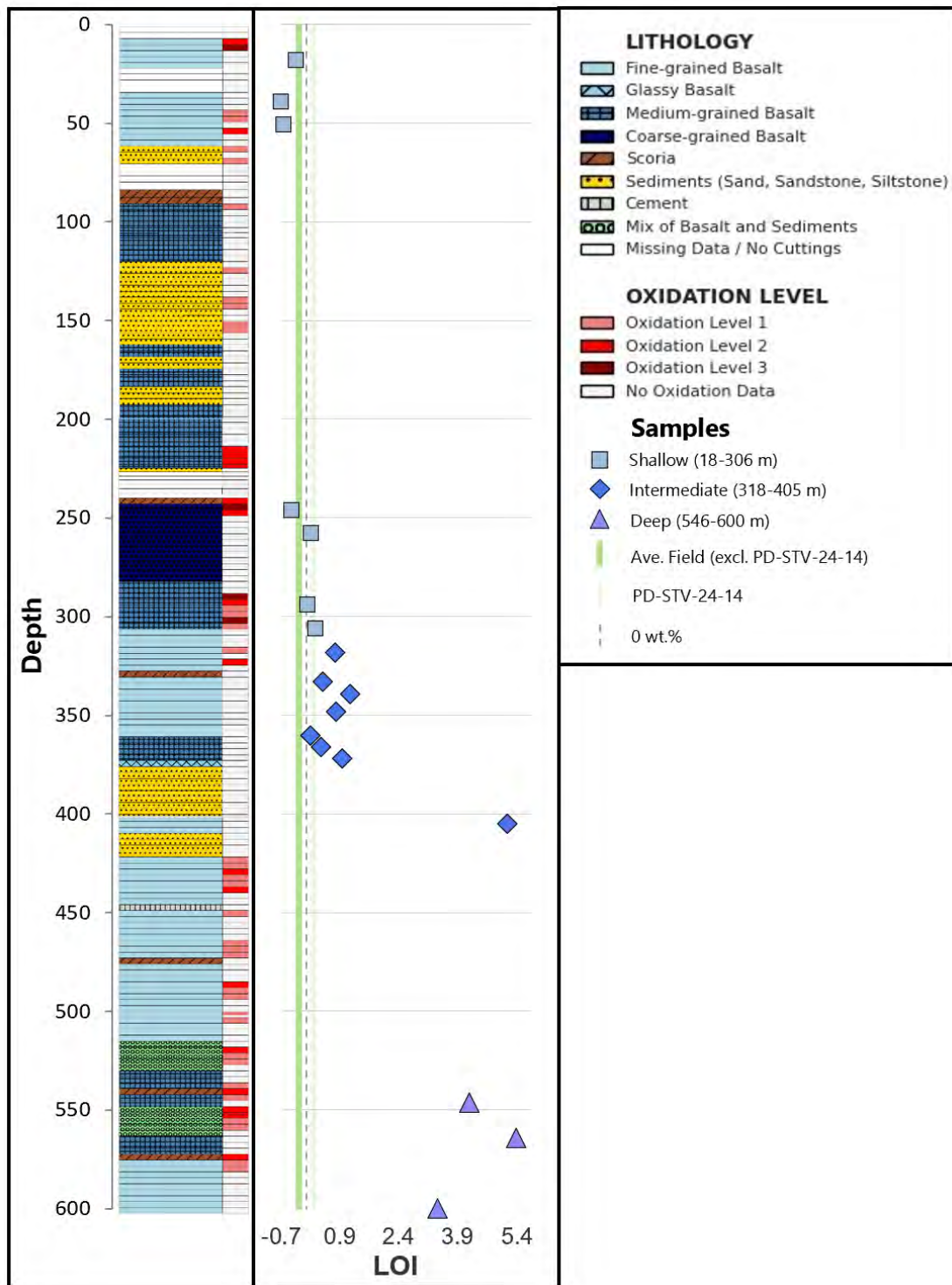


Figure 12: LOI (wt.%) plotted against depth with lithological log, shallow well samples (18-306 m) are light blue squares, intermediate well samples (318-405 m) are blue diamonds, and deep well samples (546-600 m) are purple triangles. the average of LOI values in field samples (excluding PD-STV-24-14) are shown in bright green vertical line, while the value of PD-STV-24-14 is shown in faint green vertical line; the dashed vertical line is 0 wt.%

#### 4.3.4 LOI

The LOI plot (Fig. 12) shows that while many samples have relatively low LOI content from 18 m to 306 m depth, ranging from -0.64 to 0.23 wt.%, the deeper samples from 405 m to 600 m range from 3.35 to 5.32 wt.% and show significantly higher LOI values. The intermediate well samples show 0.09 to 1.11 wt.%. The average of the field samples is -0.19 wt.% and samples from depths of 39 m, 51 m, and 246 m show even lower values of -0.64, -0.58, -0.37 wt.%. The general trend shows that the LOI content increases with depth from -0.26 wt.% at 18 m to 3.35 wt.% at 600 m.

### 4.4 Normative Calculations and Point Counting

#### 4.4.1 CIPW normative calculations

The CIPW normative mineralogy, calculated from the whole-rock geochemistry (Table 1), reveals that all samples are olivine-normative tholeiitic basalts, consistent with the AFM diagram (Fig. 10). Normative plagioclase is the most abundant mineral, typically ranging from approximately 49.0 wt.% to 58.5 wt.%. Normative clinopyroxene (diopside) is consistently high, varying from 16.4 wt.% to 23.3 wt.%. Normative orthopyroxene (hypersthene) is also present in all samples, with amounts from 2.3 wt.% to 17.9 wt.%. All samples contain normative olivine ranging from 2.4 wt.% to a significant 15.1 wt.%.

Normative values of oxides of ilmenite vary from 0.7 wt.% to 3.8 wt.%, and magnetite ranges from 0.8 wt.% to 1.4 wt.%. Normative orthoclase is generally low, between 0.3 wt.% and 1.8 wt.%, and normative apatite is a minor component, from 0 wt.% to 0.6 wt.%.

The deep-well samples (CSM-01-546m, -564m, -600m) exhibit distinct normative characteristics: they generally have the highest normative plagioclase contents (56.3 to 58.5 wt.%), very low normative oxides for ilmenite (0.7 to 1.1 wt.%) and magnetite (0.8-0.9 wt.%), and very low or absent apatite (0-0.1 wt.%). These deep-well samples also tend to show higher normative olivine (10.5-14.3 wt.%) and relatively lower normative hypersthene, particularly for CSM-01-564m (2.58 wt.%). In contrast, the field samples (PD-STV series) and the shallow to intermediate well cuttings generally show higher normative ilmenite, orthoclase, and apatite and more variable olivine and hypersthene proportions compared to the deep-well cuttings. For instance, PD-STV-24-14 has among the highest normative olivine (12.2 wt.%) for a field sample, comparable to some deeper CSM-01 samples, but with higher ilmenite (2.2 wt.%).

Table 1: CIPW normative calculation results of samples (vol.%). Abbreviations: plag: plagioclase, or: orthoclase, di: diopside, hy: hypersthene, ol: olivine, ilm: ilmenite, mag: magnetite, ap: apatite, adding up to 100% volume.

<b>Samples</b>	<b>plag</b>	<b>or</b>	<b>di</b>	<b>hy</b>	<b>ol</b>	<b>ilm</b>	<b>mag</b>	<b>ap</b>
<b>CSM-01-18m</b>	53.4	1.0	22.6	13.6	6.4	1.8	1.1	0.2
<b>CSM-01-39m</b>	53.2	1.2	21.9	17.9	2.6	1.9	1.2	0.2
<b>CSM-01-51m</b>	53.7	1.1	22.8	16.6	2.7	1.8	1.1	0.2
<b>CSM-01-246m</b>	51.7	1.8	22.5	10.2	8.2	3.8	1.3	0.5
<b>CSM-01-258m</b>	51.6	1.4	19.2	9.8	12.9	3.3	1.3	0.5
<b>CSM-01-294m</b>	51.5	1.6	21.9	11.0	9.0	3.4	1.3	0.5
<b>CSM-01-306m</b>	53.6	1.4	20.8	5.0	15.1	2.7	1.2	0.4
<b>CSM-01-318m</b>	52.8	1.3	21.3	9.7	10.6	2.7	1.2	0.4
<b>CSM-01-333m</b>	53.3	1.1	21.3	7.6	12.6	2.7	1.2	0.4
<b>CSM-01-339m</b>	52.6	0.9	20.1	13.1	8.1	3.5	1.3	0.5
<b>CSM-01-348m</b>	51.6	1.1	19.9	12.7	9.5	3.4	1.3	0.5
<b>CSM-01-360m</b>	49.0	1.2	20.9	10.0	13.7	3.4	1.4	0.5
<b>CSM-01-366m</b>	53.0	1.1	21.0	11.4	8.2	3.6	1.3	0.5
<b>CSM-01-372m</b>	53.2	1.2	21.8	12.0	6.3	3.7	1.3	0.6
<b>CSM-01-405m</b>	53.9	1.4	18.7	16.1	5.7	2.7	1.2	0.4
<b>CSM-01-546m</b>	56.3	0.4	22.8	5.5	13.2	1.0	0.9	0.1
<b>CSM-01-564m</b>	58.5	0.3	22.7	2.3	14.7	0.7	0.8	0.0
<b>CSM-01-600m</b>	57.0	0.3	20.8	8.7	11.0	1.1	0.9	0.1
<b>PD-STV-24-01</b>	52.6	1.3	23.0	17.5	2.4	1.9	1.2	0.3
<b>PD-STV-24-03</b>	52.8	1.2	23.3	16.2	3.2	1.9	1.2	0.3
<b>PD-STV-24-05</b>	53.9	1.0	22.6	14.8	4.7	1.7	1.1	0.2
<b>PD-STV-24-08</b>	54.7	1.0	21.7	16.2	3.4	1.8	1.1	0.2
<b>PD-STV-24-09</b>	54.9	1.4	20.9	14.4	5.0	2.1	1.2	0.3
<b>PD-STV-24-11</b>	55.2	1.4	20.4	13.2	6.2	2.1	1.1	0.3
<b>PD-STV-24-14</b>	53.9	0.5	16.4	12.5	13.0	2.2	1.2	0.3

#### 4.4.2 Point Counting

Modal mineralogy determined by point counting (Table 2) reveals considerable textural and mineralogical variation among the basaltic samples, complementing the normative calculations by quantifying observed phases, including alteration products and matrix components. The definition for the groundmass was from glassy to 40  $\mu\text{m}$ , where the grains of minerals can not be reliably determined. This applied to all suites but intergranular samples had 10-20% glassy and coarse-grained samples less than 5% glassy of the groundmass counted. As for the groundmass of the glassy samples, were essentially wholly glassy (80-95%).

Overall, primary igneous minerals consist predominantly of plagioclase, pyroxene, and olivine. Modal plagioclase ranges widely from 16.2% (CSM-01-372m) to 51.4% of the area (CSM-01-246m). Pyroxene count is also highly variable, from as low as 6.6% of area (PD-STV-24-11) up to 42.0% of area (CSM-01-18m). Olivine has modal abundances from 0.6% of area (PD-STV-24-11) to a significant 21.6% of area (CSM-01-246m) (see Table 2).

The matrix components show significant variation. Groundmass also varies considerably, from being absent or minor (e.g., PD-STV-24-14, CSM-01-258m) to forming a major component (e.g., 55.4% of area in CSM-01-372m; 69.4% of area in CSM-01-39m). Opaque oxides are ubiquitously present, typically ranging from 0.2% of area to around 7.4% of area, with some samples showing higher amounts up to 13.4% of area in CSM-01-294m (see Table 2). The sum of the average of reactive phases (pyroxene, olivine, and groundmass) in the shallow well samples is 53.9% of area, in the intermediate well samples 57.5% of area, and in the deep-well samples 43.9% of area. While field samples have a sum of 53.9% of the average.

General alteration products (Alt.) in field and shallow well samples are from low 0.0% to 4.4% and intermediate well samples are more pervasive and prominent in the deep-well samples, where they range from 17.0% of the area (CSM-01-546m) to 35.0% of the area (CSM-01-600m). Other samples, such as CSM-01-339m (13.6% of area) and CSM-01-405m (15.4% of area), also show substantial alteration.

Table 2: Modal mineral compositions (area%) from point counting. Abbreviations: plag: plagioclase, px: pyroxene, ol: olivine, gm: groundmass, ox: opaque oxides, alt: other alteration products.

Sample	plag	px	ol	gm	ox	alt
CSM-01-18m	31.4	41.0	6.0	17.2	4.0	0.4
CSM-01-39m	19.4	10.0	0.8	69.4*	0.2	0.2
CSM-01-51m	43.2	42.0	5.6	6.0	3.2	0.0
CSM-01-246m	51.4	17.4	21.6	2.0	6.6	1.0
CSM-01-258m	48.5	29.7	13.6	1.2	6.8	0.2
CSM-01-294m	50.4	27.6	4.0	0.2	13.4	4.4
CSM-01-306m	33.0	14.4	8.8	38.6	5.2	0.0
CSM-01-318m	26.8	22.0	7.4	37.6	4.4	1.8
CSM-01-333m	32.4	19.4	8.2	34.4*	3.2	2.4
CSM-01-339m	29.0	11.2	12.6	20.6	13.0	13.6
CSM-01-348m	29.2	14.6	8.6	39.6	2.0	6.0
CSM-01-360m	42.6	20.2	13.8	12.0	8.0	3.4
CSM-01-366m	40.2	21.8	9.8	15.6	6.6	6.0
CSM-01-372m	16.2	9.4	4.0	65.0*	3.4	2.0
CSM-01-405m	27.0	28.8	6.0	17.4	5.4	15.4
CSM-01-546m	21.6	22.4	2.0	29.4*	7.4	17.2
CSM-01-564m	28.6	18.6	12.4	11.0	5.8	23.6
CSM-01-600m	25.6	17.4	4.4	14.0*	3.4	35.2
PD-STV-24-01	28.0	12.4	2.2	47.2	7.0	3.2
PD-STV-24-03	47.2	32.2	3.2	8.8	7.0	1.6
PD-STV-24-05	23.6	7.6	14.0	50.6	3.2	1.0
PD-STV-24-08	49.4	21.0	10.8	13.8	5.0	0.0
PD-STV-24-09	49.4	27.4	4.8	13.2	5.2	0.0
PD-STV-24-11	27.8	6.6	0.6	63.6	1.4	0.0
PD-STV-24-14	48.6	23.6	14.0	0.0	13	0.8

**Note:** An asterisk (\*) indicates that the groundmass value includes predominantly glass. To see errors of each count go to table S5 in supplementary data.

## 5 Discussion

The success of any carbon sequestration project centres around moving the general understanding of the reactive nature of basalts to site-specific, qualitative assessment to determine the optimum formation. In this discussion the petrological characteristics of basaltic formations in Straumsvík, Iceland, are evaluated to assess their suitability for carbon sequestration in the rock within well CSM-01. The discussion focuses on mineralogy, grain size, and alteration state, comparing fresh surface samples (PD-STV-24 series) with downhole samples from the CSM-01 monitoring well and concluding by identifying the optimal injection depth for CO<sub>2</sub> within the CSM-01 monitoring well. Understanding these characteristics of the rock is fundamental to determining the true potential of these basalts for effective and long-term carbon storage. But firstly, lithology is discussed in the context of fluid flow, as circulation of fluid is essential to fluid-rock interaction.

### 5.1 Lithological Characterisation and Implications for Fluid Flow

The stratigraphy of the CSM-01 monitoring well consists of fine- to medium-grained basalt flows interlayered with sediment horizons and scoriaceous layers (see Section 4.1). A short interpretation of the environment that the stratigraphy formed in is given. Based on the observation of fine-grained lava flows and repeated encounters with shells in sediments, it is interpreted that the sediments were deposited near a beach environment where the well cuts through the stratigraphy. The high oxidation states found and fine-grained to glassy basalts, and mixing with sediments indicate that the lava flows went over the water-saturated sediments. This general lithology is comparable to the field samples collected (PD-STV-24 series), which often exhibited significant vesicularity (e.g., PD-STV-24-01). The presence of vesicular textures in basalts, along with rubbly or scoriaceous flow tops and bottoms, typically contributes to higher porosity and permeability (O. Sigurdsson & Stefansson, 2002). These features, coupled with fractures and the boundaries between successive lava flows, are crucial for CO<sub>2</sub>-charged fluid migration and subsequent fluid-rock interaction. Although coarse-grained massive basalt in the depth between 245 m and 282 m shows great resemblance to the coarse-grained interstadial sample PD-STV-24-14, they indicate a lower porosity and permeability due to the low vesicularity and thickness of the unit. Reports on the hydrodynamics and broader lithology for a potential Coda terminal project in the Straumsvík area suggest that such porosity and permeability are likely sufficient within the stratigraphy for efficient fluid migration and fluid-rock interaction, with flow points between 340-380 m depth (Helgadóttir et al., 2023, Sigurgeirsson et al., 2024). The presence of multiple flow units, as indicated by the lithological log of CSM-01 (Fig. 5), implies numerous interflow boundaries that can act as preferential pathways for injected fluids.

## 5.2 Mineralogy and its Suitability for Carbon Sequestration

The suitability of basaltic rocks in carbon sequestration does not simply show in the geochemistry of the rock normative calculations of minerals. Carbon sequestration is strongly dependent on their real primary mineralogy, specifically the abundance of mineral phases rich in divalent cations ( $\text{Ca}^{2+}$ ,  $\text{Mg}^{2+}$ ,  $\text{Fe}^{2+}$ ) that can react with dissolved  $\text{CO}_2$  to form stable carbonate minerals (Matter et al., 2016; Snæbjörnsdóttir et al., 2020). The primary igneous minerals observed in both field and well samples from Straumsvík consist predominantly of plagioclase, pyroxene (clinopyroxene and orthopyroxene), olivine, and variable amounts of basaltic glass and Fe-Ti oxides (Section 4.2, Table 2).

Of these, olivine, pyroxene, and glass are the most reactive phases for  $\text{CO}_2$  mineralisation (Oelkers and Gislason, 2001; Gislason and Oelkers, 2003; Heřmanská et al., 2022). The point counting data (Table 2, Section 4.4.2) and the geochemical results (Section 4.3) present an overview of their abundance. The intermediate depth zone in CSM-01 (318-405 m), which includes the permeable zone (340-380 m), shows a favourable mineral composition. For example, samples from this interval (e.g., CSM-01-318m to CSM-01-372m) show significant modal abundances of pyroxene (average  $\sim 18\%$ ) and olivine (average  $\sim 7\text{-}9\%$ ), with glassy devitrified groundmass also present, particularly in finer-grained or glassy samples (e.g., groundmass percentages in CSM-01-372m are 65% and in CSM-01-333m are 34.4%). This composition is broadly comparable to the fresh field samples (PD-STV-24 series), which, on average, also contain substantial reactive phases (e.g., PD-STV-24-05: olivine 14.0%, pyroxene 7.6%; PD-STV-24-08: olivine 10.8%, pyroxene 21.0%). The sum of the average reactive mineral in each depth interval of the well, given that groundmass is a reactive phase, is over 50% of the rocks, with the exception of the samples from the coarse-grained sample suite of 246-294 m (ave. 39.1%) and 360 and 366 m (ave. 46.6%).

The whole-rock geochemistry (Figs. 9 and 11 in Sections 4.3.1 and 4.3.3) confirms that these basalts are tholeiitic and generally rich in CaO (11.14-13.55 wt.%),  $\text{FeO}_{\text{total}}$  ( $\sim 10\text{-}14$  wt.% as FeO), and MgO (7.62-10.40 wt.%), a consistently high concentration of divalent cations ( $>30$  wt.%) is a strong indicator of the material's high potential for carbon mineralisation. The CIPW normative calculations based on the whole-rock chemistry (Table 1 in Section 4.4.1) consistently show olivine-normative tholeiites, with normative olivine ranging from 2.4 wt.% to 15.1 wt.%, and high normative pyroxene (Diop and Hy). The negative LOI values of field and shallow well samples (18-51 m). That can be an indicator that the samples oxidised, hinting at an abundance of fresh primary minerals like pyroxene or olivine within those groups (Section 4.3.4, Fig. 12).

Samples can be qualitatively ranked based on their mineralogy:

**High suitability:** The samples from the first 51 m of the well, the intermediate well samples from the permeable zone (318-372 m), and the fresh field samples (PD-STV-24 series) rank highest due to the significant presence of reactive olivine, pyroxene, and glassy groundmass.

**Moderate suitability:** Shallower well sections (246-306 m) also show good reactive

mineral content, though glass and fine-grained groundmass may be absent.

Variable to lower suitability: Deeper well samples (>405 m, e.g., CSM-01-546m, -564m, -600m) show distinct geochemical signatures (Section 4.3.3) While high olivine is good, the overall context, including alteration (see Section 5.3 below), needs consideration. The petrography of these deeper samples signalled more alteration and mixing of rocks of separate origins (Fig. 11).

This discrepancy is not an analytical error; it demonstrates that a significant portion of the mineral-forming chemistry is locked within rapidly quenched, high-surface-area glass and cryptocrystalline groundmass. For carbon sequestration, this is a highly favourable outcome. It implies that the rock's reactive components are in their most kinetically available form, suggesting that initial reaction rates could be far more rapid than in a coarse-grained, holocrystalline equivalent with the same bulk chemistry.

Conversely, the stark enrichment of modal olivine relative to the norm in samples like CSM-01-246m (21.6% modal vs. 8.2% normative) provides strong evidence for crystal accumulation. This finding is critical: it indicates that some layers are not just solidified lavas but are 'super-charged' with highly reactive olivine. While this enhances their sequestration capacity, it also implies that whole-rock chemistry alone cannot be trusted to predict the reactivity of every layer, underscoring the necessity of detailed petrographic screening.

### 5.3 Grain Size and Textural Influences on Reactivity

The texture and grain size are a significant influence on the reactivity of basaltic rocks by controlling the available surface area for fluid-rock interactions (Israeli and Emmanuel, 2018; Winter, 2010). Finer-grained and glassy basalts generally offer a much larger reactive surface area per unit volume compared to coarse-grained, holocrystalline basalts, leading to faster potential dissolution and mineralisation rates. The amorphous nature of glass provides a vastly greater reactive surface area per unit volume compared to well-crystallised equivalents (Gislason & Oelkers, 2003).

The samples were predominantly fine-grained to glassy porphyritic basalt. Three main textural suites were identified (Section 4.2): Porphyritic glassy basalts that include scoriaceous units and fine-grained basalts with a great portion of glassy or cryptocrystalline groundmass (e.g., CSM-01-39m, CSM-01-372m, PD-STV-24-11). These textures are optimal for fast reaction rates. Porphyritic intergranular basalt that are typically fine- to medium-grained with a groundmass of plagioclase, pyroxene, and some interstitial glass or cryptocrystalline material (e.g., CSM-01-18m, PD-STV-24-01, CSM-01-339m). Based on that grain size, their reactivity would be moderate to high. Coarse-grained basalts exhibit larger crystal sizes with minimal to no glass (e.g., CSM-01-246m, -258m, -294m, PD-STV-24-14). While containing reactive minerals, the larger grain size suggests a lower reactive surface area and potentially slower reaction kinetics. Phenocrysts were of similar sizes in all of the suites, with the biggest of each sample ranging from 1000  $\mu\text{m}$  to 2500  $\mu\text{m}$ .

The CIPW norm overestimates the abundance of the primary minerals relative to the

point counting, as the groundmass is of great abundance in the samples. This discrepancy between observed and normative mineralogy reflects the grain size of the samples and the potential reactive phases which are caught in the glassy or cryptocrystalline phases of high surface area, which is highly beneficial for fast reactions when the rock is in contact with fluid.

The permeable zone (340-380 m) appears to encompass a variety of these textures, including fine-grained and glassy units (e.g., scoria at 327-330 m, fine-grained/glassy basalt at 306-360 m, and glassy basalt at 372-375 m), which is favourable. The presence of highly vesicular and fine-grained zones within the stratigraphy, often associated with glassy material, would be particularly beneficial. It needs to be said that samples from depths of 360 m and 366 m are medium- to coarse-grained.

The samples can be qualitatively ranked on their grain size and texture:

Most Favourable: Units described as glassy, scoriaceous, or very fine-grained (e.g., parts of the 39 m sample, 330-360 m, 372-375 m intervals, and field samples like PD-STV-24-11).

Moderately Favourable: Fine- to medium-grained intergranular basalts, most common type throughout the well and in field samples (e.g., PD-STV-24-01, -03).

Less Favourable: Coarse-grained basalt units (e.g., 243-282 m interval, at 294 m, and PD-STV-24-14), due to less accessibility for fluid to reach reactive surface area.

#### 5.4 Alteration: Extent and Impact on Sequestration Potential

The alteration observed in the CSM-01 well serves two diagnostic purposes. First, it is like a long-term experiment showing that the primary phases are most susceptible to dissolution under the local geothermal and hydrogeological conditions. Second, it quantifies how much of the rock's primary reactive phases have been consumed by alteration and/or filled pore spaces with secondary minerals (e.g., clays, zeolites, calcite), thereby reducing both reactivity and permeability (Marieni et al., 2021).

This area of study is not highly altered, and most phenocrysts only have a limited amount of alteration, if any, though some samples show a greater degree of alteration. Groundmass was more affected by alteration than phenocrysts, but due to their cryptocrystalline nature, it was hard to estimate. The degree of alteration in these samples seems to not have affected porosity very much, as alteration has not completely filled pore spaces. The lithological logging (Section 4.1), petrographic analysis (Section 4.2), and point counting (Section 4.4.2) indicate that alteration in the Straumsvík basalts is generally minor to moderate in the upper and intermediate sections of the CSM-01 well, becoming more noticeable at greater depths (405-600 m). Oxidation is a common alteration feature, particularly close to lithological boundaries (Fig. 5, Section 4.1). Clay minerals, silica, and minor zeolites were observed. The LOI values (Section 4.3.4, Fig. 12) provide a proxy for the degree of hydration and volatile content. Relatively low LOI values (typically <1 wt.% and often negative or near zero) were observed for many samples from 18 m down to approximately 372 m, suggesting limited hydrous alteration. Negative values can be due to either reducing Fe after the heating of the

sample or errors in weighing temperature (Lechler & Desilets, 1987). If the former is true that shows that there is plenty of readily available ferrous iron in the samples. However, samples from the intermediate zone (318-372 m) showed LOI values from 0.09 to 1.11 wt.%, while deeper samples (405 m to 600 m) exhibited significantly higher LOI values (3.35 to 5.32 wt.%), indicating more substantial alteration.

Petrographically, samples from the permeable zone (340-380 m), like CSM-01-333m (2.4% alteration), CSM-01-348m (6.0% alteration), and CSM-01-372m (2.0% alteration) show relatively low amounts of alteration products (Table 2). Preservation of reactive minerals with minimal alteration is excellent (average 5% secondary minerals), and low oxidation is the predominant way of alteration for the 318-372 m interval. One outlier of alteration is CSM-01-339m which showed above average LOI content (see Fig. 12, Section 4.3.4) in the point count (13.6%) and showed iddingsite vein alterations (Section 4.2.2). Indicating a fluid pathway, a fracture or a fault. In contrast, deeper samples like CSM-01-405m (15.4% alteration) CSM-01-546m (17.2% alteration), CSM-01-564m (23.6% alteration), and CSM-01-600m (35.2% alteration) show pervasive alteration, which would likely reduce their effectiveness for sequestration. These samples are from zones of mixed lithology as they exhibit great variation of lithological grains within their thin-sections and is consistent with their high LOIs (Section 4.2). Regarding a qualitative ranking based on alteration states:

Most favourable (least altered): Fresh field samples. Shallow well sections (<306 m) also generally show low alteration.

Moderately favourable: Some intervals within the shallow to intermediate depths might show localised moderate alteration. Like at 294 m showing slight oxidation, 348 m, and 366 m (both 6% alteration of area)

Least favourable (most altered): Deeper well sections (>405 m), which exhibit higher LOI values and more extensive secondary mineralisation. and 339 m, which showed the above-average LOI content (see Fig. 12, Section 4.3.4) within the and high alteration in the point count (13.6%) and showed iddingsite vein alterations (Section 4.2.2).

### 5.5 Synthesis: Optimal Depths and Formations for Carbon Sequestration in Straumsvík

The integrated petrological analysis establishes that the basaltic formations within the Straumsvík area have considerable promise for in-situ CO<sub>2</sub> mineralisation, where the optimal target for carbon sequestration in the CSM-01 well is the 318-372 m interval. This is not a conclusion based on one parameter but the convergence of evidence pointing at the suitability of this zone. The zone consists of high abundance of reactive phases of fine-grained texture and largely preserved primary mineralogy. The zone additionally lies above the threshold of more pervasive hydrothermal alteration (e.g., below 405 m).

It is rich in olivine and pyroxene and contains glass, providing abundant divalent cations necessary for carbonate formation; therefore, it has beneficial reactive mineralogy. In grain size and texture, it includes fine-grained and glassy units and high accessibility for fluid to reach reactive surface areas, alongside medium-grained sections

Table 3: Qualitative ranking of basalt units in CSM-01 and field samples for carbon sequestration potential. Where reactive mineralogy, grain size/texture, alteration state, and overall suitability are described in terms of suitability, VH: very high suitability H: high suitability, M: moderate suitability, L: low suitability, and V: variable (Based on data in Results). The colours correspond to the ranking: bright green is high suitability, olive green is moderate to good suitability, orange is moderate suitability and grey is variable and less suitable.

Depth Interval	Reactive Mineralogy	Grain Size/Texture	Alteration State	Overall Suitability
Field Samples	H	M-H	VH	H
<51 m	H	M-H	H	H
51-306 m	M	M	H	M
<b>318-372 m</b>	<b>H</b>	<b>M-H</b>	<b>M-H</b>	<b>M-H</b>
>372 m	V	V	M	L-M

that still provide good reactivity. The alteration state is minimal, meaning that primary reactive minerals are largely preserved and porosity is less likely to be occluded by extensive secondary mineralisation. The predominantly reduced state is also favourable.

The petrological characteristics of this target zone are very similar to the fresh, highly reactive surface basalt analogues from the PD-STV-24 series, suggesting that these subsurface units will likely behave favourably upon interaction with CO<sub>2</sub>-charged water. The lithological variability within this zone, including flow boundaries and scoriaceous layers, should also provide adequate permeability for fluid injection and dispersal.

Shallower formations (<306 m) also present good potential, though perhaps with slightly more variability in glass content or localised alteration compared to the prime target zone. Deeper formations (>405 m) are generally less favourable due to more extensive alteration, despite some intervals potentially having high primary olivine content.

Table 3 summarises the integrated assessment. The intermediate zone (318-372 m) clearly emerges as the most promising interval for carbon sequestration efforts in Straumsvík based on its intrinsic petrological properties. In addition, the casing of the well is down to 223 m depth, and above that, injection cannot be executed. The petrological characteristics identified in the Straumsvík basalts, particularly in the 318-372 m interval, suggest a high intrinsic potential for CO<sub>2</sub> mineralisation, comparable to that observed in other successful basalt sequestration sites.

## 5.6 Limitations of the Study

Several limitations should be considered when interpreting the results of this study:

1. **Reliance on Cuttings:** The majority of the subsurface samples were drill cuttings. This introduces the potential for mixing of material from different stratigraphic horizons ( e.g. samples of depths 405 m, 546 m, 564 m, and 600 m), caving from uphole, and loss of crucial textural context, especially regarding vesicularity,

fracture networks, and the exact nature of flow boundaries. Also the fact that 18 samples were analysed within the 600 m deep well gave limited resolution of the stratigraphy and its potential suitable sequestration zones.

2. **Permeability/Porosity Extrapolation:** While lithology and texture provide qualitative insights, precise permeability and porosity values, critical for injectivity and fluid flow modelling, cannot be accurately determined from petrological analysis of cuttings alone.
3. **Representativeness of Point Counting:** For cuttings, especially those from coarser-grained or heterogeneously altered units, obtaining statistically representative modal mineralogy via point counting can be challenging due to the small size and fragmented nature of the samples.
4. **LOI Determination:** While LOI is a useful proxy for alteration, variations in oven temperature control or atmospheric interaction during cooling could introduce minor inaccuracies.
5. **Whole-Rock Geochemistry Averaging:** For samples that might represent a mix of different lithologies (e.g., basalt fragments and interbedded sediments from cuttings), whole-rock geochemical data will represent an average composition, potentially masking the true chemistry of the target basalt.
6. **Distinguishing Primary vs. Secondary Phases:** In some altered samples, unequivocally distinguishing fine-grained primary Fe-Ti oxides from secondary alteration oxides or devitrified glass from finely altered groundmass can be difficult through optical microscopy alone.

Despite these limitations, the consistent trends observed across multiple analytical techniques (lithological logging, petrography, geochemistry, and normative calculations) provide a robust foundation for assessing the sequestration potential.

## 6 Conclusions and Recommendations

### 6.1 Conclusions

1. The basaltic formations in the Straumsvík area, within the CSM-01 well, possess favourable petrological characteristics for carbon sequestration via in-situ mineralisation.
2. The stratigraphic interval between 318 and 372 m in CSM-01 is identified as the most promising injection zone because of its high abundance of reactive primary minerals, fine-to-medium grain sizes with glassy textures conducive to rapid reaction rates, and excellent preservation ensuring high reactivity and likely favourable porosity/permeability.
3. The petrology of this target zone is comparable to fresh surface basalt analogues and aligns well with characteristics of basalts at successful carbon sequestration sites like Carbfix.

### 6.2 Recommendations for Future Work

To further confirm the feasibility and to reduce the risk of any future sequestration project in the Straumsvík area, the following studies are recommended:

1. **Pilot Injection Test:** A small-scale pilot injection test within the 318-372 m zone would be the ultimate step to confirm in-situ reaction rates, mineralisation efficiency, and overall system under real circumstances. This could build upon the modelling and experimental insights gained from studies similar to those at Nesjavellir or other CarbFix projects (Matter et al., 2016; Galeczka, 2023).
2. **Core Drilling and Analysis:** If future project development is ever considered, obtaining continuous core through the target formations would be invaluable for detailed characterisation of textures, fracture networks, vesicularity, and direct measurement of physical properties (porosity, permeability). This could be interesting if, after the pilot project of injection is done, another core nearby could be sampled and compared to this preliminary study pre-injection analysis.
3. **Experimental Fluid-Rock Interaction Tests:** Conduct laboratory experiments using rock samples from the identified target zone (318-372 m) and CO<sub>2</sub>-charged fluids representative of potential injection conditions. This will help quantify reaction rates, secondary mineral precipitation, and changes in porosity/permeability.

These future steps would provide the necessary data to move from a petrologically favourable assessment to a fully engineered and monitored carbon storage solution.

## References

- Alcalde, J., Flude, S., Wilkinson, M., Johnson, G., Edlmann, K., Bond, C. E., Scott, V., Gilfillan, S. M. V., Ogaya, X., & Haszeldine, R. S. (2018). Estimating geological CO<sub>2</sub> storage security to deliver on climate mitigation [Publisher: Nature Publishing Group]. *Nature Communications*, *9*(1), 2201. <https://doi.org/10.1038/s41467-018-04423-1>
- Bodnar, R. J., Steele-MacInnis, M., Capobianco, R. M., Rimstidt, J. D., Dilmore, R., Goodman, A., & Guthrie, G. (2013). PVTX Properties of H<sub>2</sub>O-CO<sub>2</sub>-“salt” at PTX Conditions Applicable to Carbon Sequestration in Saline Formations. *Reviews in Mineralogy and Geochemistry*, *77*(1), 123–152. <https://doi.org/10.2138/rmg.2013.77.4>
- Er i Geochemistry of geologic co<sub>2</sub> seq depaolo.
- Calvin, K., Dasgupta, D., Krinner, G., Mukherji, A., Thorne, P. W., Trisos, C., Romero, J., Aldunce, P., Barrett, K., Blanco, G., Cheung, W. W., Connors, S., Denton, F., Diongue-Niang, A., Dodman, D., Garschagen, M., Geden, O., Hayward, B., Jones, C., . . . Péan, C. (2023, July). *IPCC, 2023: Climate Change 2023: Synthesis Report. Contribution of Working Groups I, II and III to the Sixth Assessment Report of the Intergovernmental Panel on Climate Change [Core Writing Team, H. Lee and J. Romero (eds.)]. IPCC, Geneva, Switzerland.* (tech. rep.) (Edition: First). Intergovernmental Panel on Climate Change (IPCC). <https://doi.org/10.59327/IPCC/AR6-9789291691647>
- Clark, D. E., Oelkers, E. H., Gunnarsson, I., Sigfússon, B., Snæbjörnsdóttir, S. Ó., Aradóttir, E. S., & Gíslason, S. R. (2020). CarbFix2: CO<sub>2</sub> and H<sub>2</sub>S mineralization during 3.5years of continuous injection into basaltic rocks at more than 250°C. *Geochimica et Cosmochimica Acta*, *279*, 45–66. <https://doi.org/10.1016/j.gca.2020.03.039>
- Delerce, S., Pascale, B., Jacques, S., & Eric, O. (2024). The dissolution rates of naturally altered basalts at pH 3 and 120 °C: Implications for the in-situ mineralization of CO<sub>2</sub> injected into the subsurface | Request PDF. *ResearchGate*. <https://doi.org/10.1016/j.chemgeo.2023.121353>
- Deng, H., Bielicki, J. M., Oppenheimer, M., Fitts, J. P., & Peters, C. A. (2017). Leakage risks of geologic CO<sub>2</sub> storage and the impacts on the global energy system and climate change mitigation. *Climatic Change*, *144*(2), 151–163. <https://doi.org/10.1007/s10584-017-2035-8>
- Denk, T., Grímsson, F., Zetter, R., & Símonarson, L. (2011, February). Introduction to the Nature and Geology of Iceland. [https://doi.org/10.1007/978-94-007-0372-8\\_1](https://doi.org/10.1007/978-94-007-0372-8_1)
- Einarsson, P. (2008). Plate boundaries, rifts and transforms in Iceland. *Jökull*, *58*(1), 35–58. <https://doi.org/10.33799/jokull2008.58.035>
- Einarsson, P., & Imsland, P. (2013). Náttúruvá á íslandi: Eldgosaannáll. In B. Bessason, J. Sólmes, & F. Sigmundsson (Eds.), *Náttúruvá á íslandi* (pp. 178–179). Háskólaútgáfan.

- Einarsson, S., Johannesson, H., & Sveinbjornsdottir, A. E. (1991). Krisuvikureldar II. Kapelluhraun og gatan um aldur Hellnahrauns. *Jökull*, 41, 61–80. Retrieved April 7, 2025, from <http://www.scopus.com/inward/record.url?scp=0026361734&partnerID=8YFLogxK>
- Galeczka, I. M. (2023). *Geochemical Model of the Coda Injection Reservoir* (tech. rep.). Carbfix.
- Galeczka, I. M., Stefánsson, A., Kleine, B. I., Gunnarsson-Robin, J., Snæbjörnsdóttir, S. Ó., Sigfússon, B., Gunnarsdóttir, S. H., Weisenberger, T. B., & Oelkers, E. H. (2022, March). *A pre-injection assessment of CO<sub>2</sub> and H<sub>2</sub>S mineralization reactions at the Nesjavellir (Iceland) geothermal storage site* (tech. rep.). Retrieved October 14, 2024, from <https://www.sciencedirect.com/science/article/pii/S1750583622000299>
- Gee, M. A. M., Thirlwall, M. F., Taylor, R. N., Lowry, D., & Murton, B. J. (1998). Crustal Processes: Major Controls on Reykjanes Peninsula Lava Chemistry, SW Iceland. *Journal of Petrology*, 39(5), 819–839. <https://doi.org/10.1093/etroj/39.5.819>
- Gislason, S. R., & Oelkers, E. H. (2003). Mechanism, rates, and consequences of basaltic glass dissolution: II. An experimental study of the dissolution rates of basaltic glass as a function of pH and temperature. *Geochimica et Cosmochimica Acta*, 67(20), 3817–3832. [https://doi.org/10.1016/S0016-7037\(03\)00176-5](https://doi.org/10.1016/S0016-7037(03)00176-5)
- Global Status of CCS Report: 2018* (tech. rep.). (2018). Global CCS Institute. Retrieved February 26, 2025, from <https://www.globalccsinstitute.com/resources/publications-reports-research/global-status-of-ccs-report-2018/>
- Golubić, S., Krumbein, W., & Schneider, J. (1979, January). Chapter 2.1 The Carbon Cycle. In P. A. Trudinger & D. J. Swaine (Eds.), *Studies in Environmental Science* (pp. 29–45, Vol. 3). Elsevier. [https://doi.org/10.1016/S0166-1116\(08\)71053-7](https://doi.org/10.1016/S0166-1116(08)71053-7)
- Guðnason, E. Á., & Ágústsdóttir, Þ. (2023). *Seismic Assessment in the Greater Straumsvík Area* (tech. rep.). ÍSOR. Kópavogur.
- Hansen, H., & Grönvold, K. (2000). Plagioclase ultraphyric basalts in Iceland: The mush of the rift. *Journal of Volcanology and Geothermal Research*, 98(1), 1–32. [https://doi.org/10.1016/S0377-0273\(99\)00189-4](https://doi.org/10.1016/S0377-0273(99)00189-4)
- Hardarson, B., Fitton, J., & Hjartarson, A. (2008). Tertiary volcanism in Iceland. *Jökull*, 58, 161–178. <https://doi.org/10.33799/jokull2008.58.161>
- Helgadóttir, H., Sigurgeirsson, M., Gunnarsdóttir, S., & Einarsson, G. (2023, December). *Baseline Geology and Three Dimensional Geological Model of the Straumsvík Area: Prepared for Carbfix's Coda Terminal Project for the Environmental Impact Assessment* (tech. rep.). ISOR, prepared for Carbfix.
- Heřmanská, M., Voigt, M. J., Marieni, C., Declercq, J., & Oelkers, E. H. (2022). A comprehensive and internally consistent mineral dissolution rate database: Part I: Primary silicate minerals and glasses. *Chemical Geology*, 597, 120807. <https://doi.org/10.1016/j.chemgeo.2022.120807>

- Hjartardóttir, Á. R., Einarsson, P., Magnúsdóttir, S., Björnsdóttir, Þ., & Brandsdóttir, B. (2016). Fracture systems of the Northern Volcanic Rift Zone, Iceland: An on-shore part of the Mid-Atlantic plate boundary [Publisher: The Geological Society of London]. *Geological Society, London, Special Publications*, 420(1), 297–314. <https://doi.org/10.1144/SP420.1>
- Hollocher, K. (2004). CIPW Norm Calculation Program.
- Howell, S. M., Ito, G., Breivik, A. J., Rai, A., Mjelde, R., Hanan, B., Sayit, K., & Vogt, P. (2014). The origin of the asymmetry in the Iceland hotspot along the Mid-Atlantic Ridge from continental breakup to present-day. *Earth and Planetary Science Letters*, 392, 143–153. <https://doi.org/10.1016/j.epsl.2014.02.020>
- Israeli, Y., & Emmanuel, S. (2018). Impact of grain size and rock composition on simulated rock weathering [Publisher: Copernicus GmbH]. *Earth Surface Dynamics*, 6(2), 319–327. <https://doi.org/10.5194/esurf-6-319-2018>
- Jakobsson, S., Jónasson, K., & Sigurdsson, I. (2008). The three igneous rock series of Iceland. *Jökull*, 58, 117–138. <https://doi.org/10.33799/jokull2008.58.117>
- Jakobsson, S., Jonsson, J., & Shido, F. (1978). Petrology of the Western Reykjanes Peninsula, Iceland. *Journal of Petrology*, 19(4), 669–705. <https://doi.org/10.1093/petrology/19.4.669>
- Johannsen, A. (1931). *A descriptive petrography of the igneous rocks*. University of Chicago Press. <https://catalog.hathitrust.org/Record/001488138>
- Kristjánsdóttir, H., Arnardóttir, A. R., & Logason, T. Þ. (2024). *Coda Terminal – Umhverfismatsskýrsla* (tech. rep.). Efla.
- Le Bas, M. J., Le Maitre, R. W., Streckeisen, A., Zanettin, B., & IUGS Subcommission on the Systematics of Igneous Rocks. (1986). A Chemical Classification of Volcanic Rocks Based on the Total Alkali-Silica Diagram. *Journal of Petrology*, 27(3), 745–750. <https://doi.org/10.1093/petrology/27.3.745>
- Le Maitre, R. W. (2002). *Igneous Rocks: A Classification and Glossary of Terms*. Retrieved April 15, 2025, from [https://www.researchgate.net/publication/234448684\\_Igneous\\_Rocks\\_A\\_Classification\\_and\\_Glossary\\_of\\_Terms](https://www.researchgate.net/publication/234448684_Igneous_Rocks_A_Classification_and_Glossary_of_Terms)
- Lechler, P. J., & Desilets, M. O. (1987). A review of the use of loss on ignition as a measurement of total volatiles in whole-rock analysis. *Chemical Geology*, 63(3), 341–344. [https://doi.org/10.1016/0009-2541\(87\)90171-9](https://doi.org/10.1016/0009-2541(87)90171-9)
- Luhmann, A. J., Tutolo, B. M., Bagley, B. C., Mildner, D. F. R., Seyfried Jr., W. E., & Saar, M. O. (2017). Permeability, porosity, and mineral surface area changes in basalt cores induced by reactive transport of CO<sub>2</sub>-rich brine. *Water Resources Research*, 53(3), 1908–1927. <https://doi.org/10.1002/2016WR019216>
- MacLennan, J., Jull, M., McKenzie, D., Slater, L., & Grönvold, K. (2002). The link between volcanism and deglaciation in Iceland. *Geochemistry, Geophysics, Geosystems*, 3(11), 1–25. <https://doi.org/10.1029/2001GC000282>
- Marieni, C., Voigt, M., Clark, D. E., Gíslason, S. R., & Oelkers, E. H. (2021). Mineralization potential of water-dissolved CO<sub>2</sub> and H<sub>2</sub>S injected into basalts as function of

- temperature: Freshwater versus Seawater. *International Journal of Greenhouse Gas Control*, *109*, 103357. <https://doi.org/10.1016/j.ijggc.2021.103357>
- Marini, L. (2006, October). *Geological Sequestration of Carbon Dioxide: Thermodynamics, Kinetics, and Reaction Path Modeling*. Elsevier.
- Martin, E., & Sigmarsson, O. (2007). Low-pressure differentiation of tholeiitic lavas as recorded in segregation veins from Reykjanes (Iceland), Lanzarote (Canary Islands) and Masaya (Nicaragua). *Contributions to Mineralogy and Petrology*, *154*(5), 559–573. <https://doi.org/10.1007/s00410-007-0209-5>
- Matter, J. M., Stute, M., Snæbjörnsdóttir, S. Ó., Oelkers, E. H., Gislason, S. R., Aradóttir, E. S., Sigfússon, B., Gunnarsson, I., Sigurdardóttir, H., Gunnlaugsson, E., Axelsson, G., Alfredsson, H. A., Wolff-Boenisch, D., Mesfin, K., Taya, D. F. d. l. R., Hall, J., Dideriksen, K., & Broecker, W. S. (2016). Rapid carbon mineralization for permanent disposal of anthropogenic carbon dioxide emissions [Publisher: American Association for the Advancement of Science]. *Science*, *352*(6291), 1312–1314. <https://doi.org/10.1126/science.aad8132>
- McGrail, B. P., Spane, F. A., Sullivan, E. C., Bacon, D. H., & Hund, G. (2011). The Wallula basalt sequestration pilot project. *Energy Procedia*, *4*, 5653–5660. <https://doi.org/10.1016/j.egypro.2011.02.557>
- Morris, G., & Pease, V. (n.d.). *The Stockholm Petrotectonics X-ray Fluorescence Facility: Analytical Technique, Parameters, Precision and Accuracy* (tech. rep.).
- Myer, E. M., Arnaldsson, A., Berthet, J.-C., Ásmundsson, H., & Pálmarsson, S. Ó. (2024, March). *Coda Terminal. Assessment of impacts on groundwater resources* (Impact assessment No. 24.01). Vatnaskil.
- Nicholson, H. (1991). Magmatic evolution of Krafla, N.E. Iceland [Accepted: 2013-06-26T13:38:34Z Publisher: University of Edinburgh]. Retrieved May 4, 2025, from <https://era.ed.ac.uk/handle/1842/7095>
- Oelkers, E. H., & Gislason, S. R. (2001). The mechanism, rates and consequences of basaltic glass dissolution: I. An experimental study of the dissolution rates of basaltic glass as a function of aqueous Al, Si and oxalic acid concentration at 25°C and pH = 3 and 11. *Geochimica et Cosmochimica Acta*, *65*(21), 3671–3681. [https://doi.org/10.1016/S0016-7037\(01\)00664-0](https://doi.org/10.1016/S0016-7037(01)00664-0)
- Plas, L. v. d., & Tobi, A. C. (1965). A chart for judging the reliability of point counting results [Publisher: American Journal of Science]. *American Journal of Science*, *263*(1), 87–90. <https://doi.org/10.2475/ajs.263.1.87>
- Pogge von Strandmann, P. A. E., Burton, K. W., Snæbjörnsdóttir, S. Ó., Sigfússon, B., Aradóttir, E. S., Gunnarsson, I., Alfredsson, H. A., Mesfin, K. G., Oelkers, E. H., & Gislason, S. R. (2019). Rapid CO<sub>2</sub> mineralisation into calcite at the Carb-Fix storage site quantified using calcium isotopes [Publisher: Nature Publishing Group]. *Nature Communications*, *10*(1), 1983. <https://doi.org/10.1038/s41467-019-10003-8>

- Potts, P. J. (1986, January). *A handbook of silicate rock analysis* [Publisher: Chapman and Hall, New York, NY]. Retrieved May 21, 2025, from <https://www.osti.gov/biblio/6745018>
- QGIS. (2009). <http://qgis.org>
- Sæmundsson, K., Hjartarson, Á., Sigurgeirsson, M., Kaldal, I., Kristinsson, S., & Víkingsson, S. (2010). Geological Map of Southwest Iceland (2nd). <https://arcgisserver.isor.is/?lon=-21.99667&lat=64.01155&zoom=12&layers%5B%5D=satellite&layers%5B%5D=geologyDetailed>
- Sæmundsson, K. (1991). Jarðfræði Kröflukerfisins. In *Náttúra Mývatns* (pp. 24–95). Hið íslenska Náttúrufélag.
- Sæmundsson, K., Sigurgeirsson, M., & Friðleifsson, G. (2018). Geology and structure of the Reykjanes volcanic system, Iceland. *Journal of Volcanology and Geothermal Research*, 391. <https://doi.org/10.1016/j.jvolgeores.2018.11.022>
- Schilling, J.-G. (1973). Iceland Mantle Plume [Publisher: Nature Publishing Group]. *Nature*, 246(5429), 141–143. <https://doi.org/10.1038/246141a0>
- Sigmundsson, F., Einarsson, P., Hjartardóttir, Á. R., Drouin, V., Jónsdóttir, K., Árnadóttir, T., Geirsson, H., Hreinsdóttir, S., Li, S., & Ófeigsson, B. G. (2020). Geodynamics of Iceland and the signatures of plate spreading. *Journal of Volcanology and Geothermal Research*, 391, 106436. <https://doi.org/10.1016/j.jvolgeores.2018.08.014>
- Sigurdsson, I. A., Steinthorsson, S., & Grönvold, K. (2000). Calcium-rich melt inclusions in Cr-spinels from Borgarhraun, northern Iceland. *Earth and Planetary Science Letters*, 183(1), 15–26. [https://doi.org/10.1016/S0012-821X\(00\)00269-7](https://doi.org/10.1016/S0012-821X(00)00269-7)
- Sigurdsson, O., & Stefansson, V. (2002). Porosity structure of Icelandic basalt. *Proceedings of the Estonian Academy of Sciences. Geology*, 51, 33–46. <https://doi.org/10.3176/geol.2002.1.03>
- Sigurgeirsson, M., Jónsson, J., Ingólfsson, H., Kaldal, G., & Gunnarsdóttir, S. (2024, January). *Straumsvík – Well CSM-01: Drilling of Well CSM-01 from Surface down to 618 m* (tech. rep.). ISOR, prepared for Carbfix.
- Slater, L., Jull, M., McKenzie, D., & Grönvold, K. (1998). Deglaciation effects on mantle melting under Iceland: Results from the northern volcanic zone. *Earth and Planetary Science Letters*, 164(1), 151–164. [https://doi.org/10.1016/S0012-821X\(98\)00200-3](https://doi.org/10.1016/S0012-821X(98)00200-3)
- Snæbjörnsdóttir, S. Ó., Sigfússon, B., Marieni, C., Goldberg, D., Gislason, S. R., & Oelkers, E. H. (2020). Carbon dioxide storage through mineral carbonation [Publisher: Nature Publishing Group]. *Nature Reviews Earth & Environment*, 1(2), 90–102. <https://doi.org/10.1038/s43017-019-0011-8>
- Solomon, S. (2007, May). *Carbon Dioxide Storage: Geological Security and Environmental Issues – Case Study on the Sleipner Gas field in Norway* (tech. rep.). Bellona.
- The International Energy Agency. (2019, September). Putting CO<sub>2</sub> to Use – Analysis. Retrieved March 31, 2025, from <https://www.iea.org/reports/putting-co2-to-use>

- The International Energy Agency. (2020, September). CCUS in Clean Energy Transitions – Analysis. Retrieved March 31, 2025, from <https://www.iea.org/reports/ccus-in-clean-energy-transitions>
- Thordarson, T., & Larsen, G. (2007). Volcanism in Iceland in historical time: Volcano types, eruption styles and eruptive history. *Journal of Geodynamics*, *43*(1), 118–152. <https://doi.org/10.1016/j.jog.2006.09.005>
- Vermeesch, P., & Pease, V. (2021). A genetic classification of the tholeiitic and calc-alkaline magma series. *Geochemical Perspectives Letters*, *19*(19), 1–6. Retrieved June 13, 2025, from <https://www.geochemicalperspectivesletters.org/article2125/>
- Wang, J., Yagi, M., Tamagawa, T., Hirano, H., & Watanabe, N. (2024). Reactivity and Dissolution Characteristics of Naturally Altered Basalt in CO<sub>2</sub>-Rich Brine: Implications for CO<sub>2</sub> Mineralization [Publisher: American Chemical Society]. *ACS Omega*, *9*(4), 4429–4438. <https://doi.org/10.1021/acsomega.3c06899>
- Winter, J. D. (2010). *An introduction to igneous and metamorphic petrology* (Vol. 2). Prentice Hall.  
2. ed., International ed.
- Wolfe, C. J., Th. Bjarnason, I., VanDecar, J. C., & Solomon, S. C. (1997). Seismic structure of the Iceland mantle plume [Publisher: Nature Publishing Group]. *Nature*, *385*(6613), 245–247. <https://doi.org/10.1038/385245a0>